Biogenic and Abiotic Carbonates in Altered Oceanic Crust (AOC) and Implications to Subduction Zone Carbon Cycle

by

Kan Li

A thesis submitted in partial fulfillment of the requirements for the degree of

Master of Science

Earth and Atmospheric Sciences
University of Alberta

Abstract

Altered oceanic crust (AOC) is an important carbon reservoir for subduction-zone carbon recycling. However, the character of the carbon reservoir (e.g., total budget and isotopic signatures) in AOC has not been well constrained. Here, based on analyses of contents and isotope compositions of 73 DSDP/ODP/IODP samples (22 pillow basalts, 7 sheeted dikes, 22 gabbros and 22 peridotites) and 7 gabbro samples from the Oman Ophiolite, we show that carbonates in gabbros and peridotites were all precipitated at near surface low temperature conditions instead of being precipitated at their corresponding depths in the deeper oceanic crust, and thus cannot represent the true values of the lower oceanic crust sections. Our modeling yielded a new value for carbon input flux in AOC of 1.3×10^{12} moles C/year, which is only 30-60% of previous estimates. We also observed that carbonate in some oceanic crust segments, such as the Cocos plate (ODP/IODP Site 1256D) and the Southwest Indian Ridge (ODP Site 735B), is predominately biogenic in origin with weighted average $\delta^{13}C$ values of -20.4‰ to -6.3‰. If such AOC is subducted and provides a carbon source for diamond formation, the diamond can inherit the "organic"-like $\delta^{13}C$ values but maintain normal mantle $\delta^{15}N$ values. This may provide an alternative explanation for the decoupled $\delta^{13}C$ and $\delta^{15}N$ signatures in some eclogitic diamonds.

Preface

Oman gabbro samples in this study were provided by Dr. Graham Pearson at the University of Alberta. Other altered oceanic crust samples were provided by IODP Kochi Core Center (KCC) in Japan, IODP Bremen Core Repository (BCR) in Germany, and IODP Gulf Coast Repository (GCR) in Texas. The author was responsible for sample preparation (e.g., sawing, crushing and weighing) and data collection (carbonate quantification and isotopic measurements), and modeling.

Carbon and oxygen isotope analysis of altered basalt, sheeted dike, gabbro and peridotite samples were conducted in Dr. Long Li's Stable Isotope Laboratory at the University of Alberta in 2016-2017.

Acknowledgement

Foremost, I would like to express my sincere gratitude to my supervisor, Dr. Long Li, for his inculcation throughout the last two years, for his valuable guidance during my first research work, for his patience and immense knowledge in teaching me how to conduct a research.

Secondly, I would like to thank Dr. D. Graham Pearson at the University of Alberta, DSDP, ODP, IODP for generously offering us those priceless samples.

Thirdly, I would like to thank the following people, for their crucial contribution during my research work in explaining analytical techniques, conducting lab works, and giving advises on my thesis: Zhe Zhang (Graduate student in Long Li's Laboratory), Dr. Karlis Muehlenbachs, Olga Lenver (Technician, Stable isotope Laboratory), Dr. D. Graham Pearson, Dr. Thomas Stachel, Yingzhou Li and Yuying Deng (Graduate students in Long Li's Laboratory).

Additionally, I would like to thank Dr. Larry M. Heaman, Dr. Jingao Liu, Dr. Long Li, for their inspiring instruction in the courses I had taken.

Last but not least, I would like to thank my parents, for their support and encouragement throughout these years.

This research is generously funded by the: Natural Sciences and Engineering Research Council.

Table of Contents

List of Tables

List of Figures

1. General Introduction

Carbon (C) uptake by alteration of oceanic crust in form of carbonate minerals makes altered oceanic crust (AOC) an important carbon reservoir, with quantity at the same order of marine sediments (Alt and Teagle, 2003; Staudigel et al., 1989), in the geological carbon cycle (Brady and Gíslason, 1997; Francois and Walker, 1992). As hydrothermal fluid comes into contact with oceanic crust, basaltic glass, olivine, and sometimes plagioclase tend to be altered, releasing cations, such as Ca^{2+}, Mg^{2+}, Fe^{2+} (Gudbrandsson et al., 2011; Wolff-Boenisch et al., 2006). A significant portion of the cations leached from oceanic basement rocks either enter fluid phase as free ions or are incorporated into secondary minerals that replace groundmass phases and fill pore space (fractures, vesicles, vugs), such as smectite, chlorite and albite (Humphris and Thompson, 1978; Seyfried Jr, 1987; Staudigel et al., 1981). Carbonate minerals are precipitated via cations (Ca^{2+}, Mg^{2+}, etc.) bound with carbonate anions in circulating seawater (Fig. 1). Whether these carbonate minerals precipitate continuously as the oceanic crust rafts away from mid-ocean ridge (Alt and Teagle, 1999) or most of them (～90%) form within ～20Ma after crustal accretion (Coogan et al., 2016) is still controversial. However, either continuous or rapid precipitation of carbonate undoubtedly leads to the carbonation of oceanic crust, which is eventually transported into subduction zones. Within subduction zones, the ultimate fate of carbonate minerals in altered oceanic crust is controlled by decarbonation, dissolution, redox transition or melting processes (Galvez et al., 2013; Gorman et al., 2006; Kelemen and Manning, 2015; Kerrick and Connolly, 2001b; Pan et al., 2013; Rohrbach and Schmidt, 2011; Thomson et al., 2016). Theoretical modelling by Kerrick and Connolly (2001b) and Molina and Poli (2000)

indicates that the degree of decarbonation is limited in cold and intermediate-geotherm subducting slabs, implying deep subduction of carbon. These carbonate minerals may mainly exist as Mg-rich carbonate minerals as a slab descends, such as dolomite and magnesite (Dasgupta and Hirschmann, 2010; Merlini et al., 2012; Poli et al., 2009). However, Pan et al. (2013) and Facq et al. (2014) show that carbonate can be soluble in subduction zone aqueous fluids. Theoretical calculation by Kelemen and Manning (2015) suggests that almost all of the subducted carbonate is transferred to lithospheric mantle and crust by carbonate dissolution. Besides carbonate dissolution, some carbon stabilizing processes can also occur in subduction zones. For example, reduction of carbonate minerals into graphite during redox transition (e.g., at the contact of mafic-ultramafic rocks) may provide a mechanism to facilitate the transportation of surficial carbon into deeper mantle (Galvez et al., 2013). Moreover, theoretical modeling by Rohrbach and Schmidt (2011) indicates that carbonates may be reduced into elemental carbon or carbides by iron metal at depths greater than 250 km, where (Fe, Ni)-metal phase may be stable (Rohrbach et al., 2007). In addition to redox control on the behavior of subducted carbonate, carbonate retained in oceanic crust may also enter melt phase as carbonatitic melt within the transition zone, and its return to the shallow depth due to low density may in turn hinder the subduction of carbonates to the lower mantle (Li et al., 2017). Studies on the refractory mantle mineral diamond show that its carbon isotopic ratio ($\delta^{13}C$) can be deviated from the main mantle range. Some diamonds are enriched in ^{13}C ($\delta^{13}C > 0‰$), compared with the main mantle range (-5±3‰) (Cartigny et al., 2014), which is taken as a direct evidence for deep recycling of sedimentary carbonate minerals ($\delta^{13}C$ ~0‰) (Palot et al., 2012; Palot et al., 2014; Stachel et al., 2002). Some diamonds are depleted in ^{13}C with $\delta^{13}C$ as low as -40‰, which has been attributed to the recycling of sedimentary organic carbon (Tappert et al., 2005; Walter et al., 2011). Both

marine carbonate-like and organic carbon-like $\delta^{13}C$ values in diamonds indicate deep subduction of surficial carbon during the geological history, which is consistent with previous and recent modeling work that subduction of surficial carbon plays a critical role in influencing the deep carbon cycle (Duncan and Dasgupta, 2017; Kerrick and Connolly, 2001a, b). However, carbon isotopic signatures of diamonds distinct from the mantle range have also been attributed to mantle heterogeneity and/or high temperature isotope fractionation (Cartigny, 2005). The conflicting results from experimental investigations, theoretical calculations and field studies exemplify the current strong debate on whether or not crustal carbon can be transported to the deep mantle. However, the majority of the previous studies consider sediment as the major crustal carbon reservoir. The carbon content and carbon isotopic characteristics of altered oceanic crust have not been well constrained due to our limited knowledge on it.

So far, most of our understanding on the mechanisms of C uptake by AOC is built on analysis of basaltic samples (mostly recovered by DSDP/ODP/IODP drillings) (Alt and Teagle, 1999; Gillis and Coogan, 2011; Staudigel et al., 1989), which are most available compared with other lithologies of oceanic crust (i.e., gabbro, sheeted dike, and peridotite). A number of previous oxygen isotope studies on carbonate veins in altered basalts indicate that C uptake by AOC is mainly at low temperatures (T) of 0-60 ºC (Fig. 2A), despite a small number of carbonate veins in serpentinized peridotites showing much lower $\delta^{18}O$ values corresponding to alteration T as high as 235 ºC (Alt and Shanks, 2003; Bach et al., 2011) (Fig. 2B). The relative contribution of high-T alteration and low-T weathering to the overall C budget in AOC is still poorly constrained. This is mainly attributed to (1) limited availability of high-T AOC samples and (2) unpaired analyses of C concentrations and isotopic compositions for most of the studied AOC samples. The lack of this key understanding severely prevents the modeling of the carbon

budget of the entire oceanic crust at a global scale. So far, samples from deeper sections of oceanic crust (i.e., gabbro, sheeted dike, and peridotite) are relatively rare and not well studied. The constraints on C budgets in these lower sections (Kelemen and Manning, 2015), where seawater alteration occurs mainly at relatively high T (>100ºC) (Staudigel, 2003), relied on a few ODP/IODP drill core samples taken from lower oceanic crust sections tectonically uplifted to near surface (Cannat et al., 1992; Cannat et al., 1995). Thinner oceanic crust induced by poor magma supply and amagmatic extension of large-scale long-lived detachment faults facilitates the exposure of these lower crust/uppermost mantle rocks (Bonatti, 1976; Cannat, 1996; Francheteau et al., 1990; Tucholke and Lin, 1994; Tucholke et al., 1998). For example, exposure of gabbroic rocks from Site 735B at the ultraslow spreading Southwest Indian Ridge is a result of poor magmatic supply and development of a detachment fault (Ildefonse et al., 2007). Lack of melt at the propagator tip of the Cocos-Nazca plate leads to the uplift of peridotite rocks at Site 895 (Francheteau et al., 1990). Hart et al. (1994) and Blusztain and Hart (1996) showed that most carbonate veins in these rocks gave high $\delta^{18}O$ values up to ~35‰, indicating very low-T C uptake (< 14 ºC), likely occurring at near surface localities after their emplacement rather than at their initial depths. However, whether the bulk carbonate (the data used for modeling the carbon budget) in these rocks is mostly low T in origin is still not known. Therefore, whether the measured C concentrations in gabbro and serpentinite samples recovered by DSDP/ODP/IODP drillings from the topmost oceanic crust are representative of those of the lower sections of oceanic crust for C budget estimate requires further test.

In this thesis, I present a detailed examination on concentrations as well as C and O isotopic compositions of bulk-rock carbonate in representative oceanic crust samples, including altered basalt, gabbro and peridotite. The result indicates that C uptake by AOC mainly occurs

during low temperature weathering processes. Based on these data, I propose a new model to estimate the C budget of oceanic crust.

2. Sample Description and Analytical Methods

2-1 Sample Description

In this study, I examined 73 shallow (0.7-1,501 meters below seafloor) AOC samples (22 pillow basalts, 7 sheeted dikes, 22 gabbros and 22 peridotites) recovered by DSDP/ODP/IODP drill cores from the Pacific, Atlantic and Indian oceans (Fig. 3), as well as 7 relatively fresh gabbro samples from the Oman Ophiolite.

Basalt samples are from ODP/IODP Hole 1256D and DSDP 543A. ODP/IODP Hole 1256D is in the crust of East Pacific Rise that was formed in ～15 Myr ago, with a superfast spreading rate of 200-220 mm/year (Fig. 3). The hole penetrated 1507 m below seafloor (mbsf), including lavas (276-1004 mbsf), transition zone (1004-1061 mbsf), the underlying sheeted dike complex (1061-1407 mbsf), and gabbroic rocks (1407-1507 mbsf) (Wilson et al., 2006). Site 1256 recovered nearly the entire section of sediment, including a clay rich layer (0-40.6 mbsf) and a carbonate layer (40.6-250.7 mbsf). $\delta^{13}C$ and $\delta^{18}O$ values of these carbonate samples range from -1.4‰ to 2.8‰ and from 28‰ to 32‰, respectively (Jiang et al., 2007). The alteration temperature is relatively low (50-125°C) in the upper lavas, and increases to 185°C at the base of the lava (Alt et al., 2010). An oxygen isotope study of vein minerals suggests a stepwise temperature increase from lava top to transition zone, which is associated with mixing between downwelling low-T seawater and upwelling high-T hydrothermal fluid (Alt et al., 2010). The secondary minerals formed by alteration of lava are dominated by saponite + pyrite, plus minor amounts of late carbonate and zeolites. The lack of oxyhydroxide alteration halos indicates a reducing alteration condition which may be related to the restriction of downwelling flow by

capping of massive ponded lava (Alt et al., 2010). The transition zone and sheeted dikes are characterized by greenschist and sub-greenschist minerals in rocks and veins, with temperature greater than 200°C. Chlorite is a major alteration phase above ～1300 mbsf, but amphibole becomes dominant below this depth. The plutonic gabbroic rocks are variably altered, with clinopyroxene in the plutonic rocks extensively being replaced by amphibole and granular magnetite. Plagioclase is generally only slightly altered to albite-oligoclase. Olivine is variably altered to smectite, chlorite, talc, magnetite (Alt et al., 2010; Wilson et al., 2006).

Hole 543A is located on the Atlantic abyssal plain (Fig. 3**)**, at 3.5km seaward of the deformation front of the Barbados Ridge complex, which was formed by the westward subduction of the Atlantic plate beneath the Caribbean plate at a subduction rate of 20 mm/year. The Campanian (～87Ma) basaltic substratum was reached at 411 m sub-bottom and drilled down to 455 m in Hole 543A (Shipboard Scientific Party., 1984). Sediment of Hole 543A mainly composes of ashy mud, ashy nannofossil mud and claystone (Shipboard Scientific Party., 1984). Some planktonic foraminifer recovered from Site 543 show $\delta^{13}C$ and $\delta^{18}O$ values from 0‰ to 3‰ and from 29‰ to 31‰, respectively (Oberhansli and Hemleben, 1984). The recovered 35.9 m basalts appear to be exclusively constituted by pillows. The alteration of the pillow lava can be divided into three stages. The first stage is dominated by the formation of celadonite, iron-hydroxide and some clay minerals, indicating an oxidative alteration. The second stage is dominated by non-oxidative pyrite precipitation and the latest stage is represented by the formation of calcite filling in the fractures and inter pillow space (Natland et al., 1984).

Gabbro samples are from Hole 735B and the Semail Ophiolite in Oman. Hole 735B, covered by thin sediment, is located at the top of a shallow uplifted Atlantis Bank, along a

transverse ridge at the Atlantis II Transform Fault in the ultraslow-spreading Southwest Indian Ridge (Fig. 3**)**. The hole extends to 1508 m into the 11.5-my-old gabbroic oceanic crust, which is exposed to seafloor by long-lived detachment faulting at the northern ridge-transform intersection (Dick et al., 1991). Hole 735B is mainly made up by ～76% of olivine gabbro suite, including olivine gabbro, troctolitic gabbro, and troctolite, and ～24% of differentiated gabbros, oxide gabbros, and felsic veins (Natland and Dick, 2002). The alteration and deformation degrees decrease with increasing depth in Hole 735B. High-T axial alteration mainly concentrates in the uppermost 300 m to 500 m of Hole 735B and off-axis low-T alteration is more intense in the lower 1000 m (Alt and Bach, 2001). Late stage carbonate veins, associated with phyllosilicates and iron oxyhydroxide, are most concentrated in the 500-600 mbsf interval, indicating low T oxidative alteration by seawater (Alt and Bach, 2001). $\delta^{18}O$ values of carbonate veins from 735B are consistent with the mineralogy, indicating a low T signature (Hart et al., 1994).

The Semail Ophiolite, which has an emplacement age of 96 – 94 Ma (Searle and Cox, 1999; Tilton et al., 1981), is considered to be formed at either the Tethyan Mid-Ocean Ridge via Cretaceous spreading in the Hawasina ocean basin (Gregory and Taylor, 1981; Tilton et al., 1981), or at a spreading center above a subduction zone associated with subduction of the Arabian oceanic crust (Dilek and Furnes, 2014; Goodenough et al., 2014; Searle and Cox, 1999). The stratigraphic section of the ~15 km Semail Ophiolite includes pillow lava (<700m thick), 1 to 2 km diabase dike complex, 1 km non-cumulate gabbro (upper gabbro), 3-5 km cumulate gabbro (lower layered gabbro), followed by the underlying mantle peridotite (Gregory and Taylor, 1981; Kelemen et al., 1997). The metamorphic facies of the Semail Ophiolite vary from zeolite facies in the upper basaltic rocks to amphibolite facies in the upper gabbro. The alteration

minerals in the lower gabbro layer are very fine and only visible under a microscope, suggesting that the alteration degree is not intense (Gregory and Taylor, 1981). However, the ^{18}O-depletion of these rocks indicates they are highly altered by fluid (Gregory and Taylor, 1981). Overall, the well preserved igneous textures in the ophiolite sequence denote that hydrothermal metamorphism is static (Gregory and Taylor, 1981).

Peridotite samples are from Holes 920D, 1271A/B, and 1274A. Hole 920D is located in the 2 km wide western median valley wall of the Mid Atlantic Ridge (MAR) and nearly 30 km south of the Kane Transform (MARK) (Shipboard Scientific Party., 1995) (Fig. 3**)**. Gabbroic rocks and peridotite (<1-Ma-old**)** are exposed near seafloor localities by lithospheric extension along a detachment fault (Karson and Lawrence, 1997). The 95.08 m recovered rocks from Hole 920D are dominantly serpentinized peridotite (95%), among which 87% is harzburgite and the remainder is dunite and lherzolite. The remaining 5% of the recovered rocks are mainly metamorphosed and deformed gabbroic rocks (Shipboard Scientific Party., 1995). The recovered rocks from Site 920 display 75%-100% alteration and are characterized by extensive development of mesh-textured serpentine and minor amounts of talc, amphibole and chlorite, with carbonate minerals formed during the latest generation of veining (Dilek et al., 1997). Serpentinization temperature of ～350°C was estimated by oxygen isotope fractionation between serpentine and magnetite (Agrinier and Cannat, 1997). However, carbonate vein $\delta^{18}O$ values from 920D show large variation from 1 to 235°C (Alt and Shanks, 2003).

Sites 1271 and 1274 were drilled on the western wall of the axial valley north (Site 1274) and south (Site 1271) of the 15°20'N Fracture Zone at the MAR during ODP Leg 209 (Fig. 3**)**. Uppermost mantle peridotites and lower crustal gabbros are exposed by crustal thinning along long-lived low-angle detachment fault (Alt et al., 2007). Holes 1271A and 1271B recovered a

mixture of ultramafic and mafic lithologies. Hole 1271A was drilled on a slope covered by thin sediment and penetrated 44.8 m into basement rocks. Approximately 5 m serpentinized peridotite was recovered, with altered dunite as the predominant lithology. Dunite is extensively replaced by serpentine and magnetite, and noticeable amounts of brucite are present in some cores. Some intervals exhibit effects of low-temperature seafloor alteration and oxidation (Fe-oxyhydroxides). Hole 1271B was drilled 74 meters southwest of Hole 1271A, and penetrated 103.6 m into a complex association of altered peridotite and gabbroic rocks. Dunite accounts for 56% in the 16 m recovered rocks, with the remaining consisting of 9% harzburgite and 35% gabbroic rocks. Black serpentine + magnetite veins are the dominant vein type in Hole 1271B, forming anastomosing networks. Other vein minerals comprise of talc, carbonate, amphibole, and minor chlorite, epidote, iron oxide, and clay. Below ～50 mbsf, mafic rocks intruded and infiltrated the ultramafic rocks, and experienced syn-deformational hydrothermal alteration to amphibolite (Shipboard Scientific Party., 2004). Hole 1274A penetrated 156 m into basement rocks and recovered 34 m rocks comprised of 77% serpentinized harzburgite, 20% dunite, and 3% gabbro. The uppermost 90 m are affected by oxidative seawater alteration, forming centimeter-wide halos (Fe-oxyhydroxide) along carbonate veins. Systematic downhole increase of alteration degree to nearly 100% serpentinization is probably associated with large faults in the lower hole section (Shipboard Scientific Party., 2004). The lower half of the hole is completely altered (>95 vol% secondary minerals) to brucite + serpentine + magnetite (Shipboard Scientific Party., 2004). Studies on Li-Sr isotope of 1271A/B and 1274A samples suggest the temperature of fluid-rock interaction is 350-400°C. However, late stage low-T aragonite precipitation indicates that carbonate minerals were mainly precipitated from ambient seawater at near seafloor localities (Bach et al., 2011).

2-2 Analytical Methods

The carbonates in AOC samples were quantified and measured for C and O isotopes by a Gasbench II system coupled with a Thermo Fisher MAT 253 isotope-ratio spectrometer (IRMS) at the University of Alberta.

Prior to sample analysis, I carefully evaluated potential oxidation of organic matter (if there is any) in the samples by H_3PO_4 acids. Several sets of testing experiments were carried out by (1) reacting varying amounts of H_3PO_4 acids with fixed amounts of samples, (2) reacting fixed amounts of H_3PO_4 acid with varying amounts of samples, (3) reacting fixed amounts of H_3PO_4 acids with fixed amounts of samples for varying reacting times. The results show no variations in either carbonate concentrations or isotopic compositions, indicating no significant CO_2 from oxidation of organic matter during carbonate extraction.

For most of the AOC samples, 50 – 1500 mg whole rock powders (depending on the in organic carbon concentration) were loaded into a glass vial. A highly pure helium stream was then introduced into the vial to remove the air. After flushing, 0.1 – 1.0 ml 100% phosphoric acid was injected into the tube to react with the powder at 72 ºC for 3 hours. Samples with mass greater than 200 mg in the vials were shaken gently after acid injection in order to ensure complete reaction between acid and powders. The produced CO_2 was then sent by a helium stream to the IRMS to measure C and O isotope compositions. During a running sequence, two NBS-18 international standards and two lab standards (LSC-1) were measured at the beginning, middle and end of the sequence to monitor data quality and long term performance of instrument. The C and O isotopic compositions are reported as δ notation relative to VPDB and VSMOW,

respectively. Carbonate in the sample was quantified using the CO_2 peak area. Analytical uncertainties are 0.2‰ for both $\delta^{13}C$ and $\delta^{18}O$, and 2% for C concentrations.

3. Results and Discussion

3-1 Positive Correlation Between Carbon and Oxygen Isotopes

$\delta^{13}C$ and $\delta^{18}O$ values of carbonate in altered basalt, sheeted dike, gabbro and peridotite are listed in Table 1 and plotted in Fig. 4.

For altered basalts (Fig. 4A), our new data from sites 504A and 1256D generally overlap with previously published data (Alt, 2003; Furnes et al., 2001; Furnes and Staudigel, 1999; Torsvik et al., 1998). Overall, the basalts show large isotopic variations from -19.7‰ to 4.6‰ for $\delta^{13}C_{carbonate}$ and from 8.3‰ to 36.5‰ for $\delta^{18}O_{carbonate}$ with a positive linear trend between $\delta^{13}C_{carbonate}$ and $\delta^{18}O_{carbonate}$ values. This positive trend can be explained by two models. The first model assumes that carbonate and seawater reached O isotope equilibrium. Consequently, the large $\delta^{18}O_{carbonate}$ variation points to carbonate deposition at a variety of T conditions from 0~220ºC, and the correlated $\delta^{13}C_{carbonate}$ variation (as low as -19.7‰) can be explained as a result of enhanced hydrothermal degradation of organic matter (OM) at elevated T. However, OM decomposition generally requires relatively high temperatures (>150°C) together with efficient mineral catalysis (Mango and Elrod, 1999; Mango and Hightower, 1997). Such high-T hydrothermal systems generally occur in or near mid-ocean ridges, where carbonate is less likely to precipitate in an acidic environment due to the OM oxidation (Froelich et al., 1979). Furthermore, very few high-T carbonate veins have been observed in AOC so far and the few veins interpreted to originate at high-T show $\delta^{13}C$ values above ~0‰ instead of organic-like signature (Alt and Shanks, 2003; Bach et al., 2011). Organic matter is depleted in high-T on axis hydrothermal system relative to off-axis low-T hydrothermal systems (Lang et al., 2006). Thus,

progressive hydrothermal degradation of OM at elevated T is an unlikely mechanism to explain the correlated decrease in $\delta^{13}C_{carbonate}$ and $\delta^{18}O_{carbonate}$.

Instead, the obvious decoupling of $\delta^{13}C$ and $\delta^{18}O$ values between bulk rock and carbonate vein (Fig. 5) indicates the occurrence of strongly ^{13}C- and ^{18}O-depleted amorphous carbonate in the sample. The linear trend in Fig. 4A can be better explained by a mixing model between two end-members. The upper end-member, characterized by $\delta^{13}C_{carbonate}$ and $\delta^{18}O_{carbonate}$ values similar to marine sedimentary carbonate, has been widely observed in previous studies and explained to be formed by seawater inorganic C precipitation during low-T alteration of basalts (Coggon et al., 2004). This end-member is referred to as "normal carbonate" hereafter. The other end-member, which is represented by some basaltic samples from sites 396B, 896A, and 1256D and characterized by strong depletions in $^{13}C_{carbonate}$ and $^{18}O_{carbonate}$, could be possibly explained by biological effect. Furnes et al. (2001) proposed that the extremely low-$\delta^{13}C$ carbonate in basaltic samples was a product of bio-alteration of basalts, in which organic matter oxidation results in the ^{13}C-depleted carbonate. This mechanism can easily explain the extremely low $\delta^{13}C_{carbonate}$ values but has difficulties in explaining the low $\delta^{18}O_{carbonate}$ values. In order to reconcile the low $\delta^{18}O_{carbonate}$ data, those authors (Furnes et al., 2001; Torsvik et al., 1998) have to invoke complicated conditions combining hydrothermal fluids that had $\delta^{18}O$ values shifted from seawater and a high-T condition for bio-alteration.

This difficulty has now been solved by recent laboratory experiments (Thaler et al., 2017), which show that $\delta^{18}O$ values of biogenic carbonates can display ^{18}O depletion by 16-25‰ relative to normal carbonate in equilibrium with ambient water (Kim and O'Neil, 1997). Assuming that the carbonate veins with seawater carbonate-like $\delta^{13}C$ (~0‰) and $\delta^{18}O$ (~32‰)

values are precipitated at isotope equilibrium with seawater with $\delta^{18}O$ = 0‰ (Fig. 5), the oxygen isotope difference between bulk rock carbonate and carbonate veins at each site varies from 0‰ to 27‰. The largest isotope difference between bulk rock carbonate and carbonate veins of each sites ranges from 14‰ to 27‰, consistent with a range from 16.0‰ to 24.7‰ observed in the experiments by Thaler et al. (2017). Experimental work by Mortimer and Coleman (1997) also suggests that biogenic siderites produced by Fe(III) reducing microorganisms show obvious ^{18}O depletion of up to 10‰, and natural siderites in banded iron formation (BIF) show ^{18}O depletion of up to 9‰ (Heimann et al., 2010). Mortimer and Coleman (1997) did not give a specific explanation for oxygen isotope disequilibrium in the experiment, but Heimann et al. (2010) attributed the low $\delta^{18}O_{siderite}$ values to the contribution of ^{18}O-depleted oxygen from iron-hydroxide during dissimilatory iron reduction (DIR) processes. As noted by Thaler et al. (2017), the oxygen isotope disequilibrium between DIC and water in their experiments may be inherited from the kinetic isotope effect associated with CO_2 hydration/hydroxylation (hydration: $CO_2 + H_2O = HCO_3^- + H^+$; hydroxylation: $CO_2 + OH^- = HCO_3^-$), which have long been regarded as important factors for oxygen isotope disequilibrium in some biological carbonates (McConnaughey, 1989a, b; McConnaughey, 2003; Rollion-Bard et al., 2003). For example, Rollion-Bard et al. (2003) attributed the micrometer scale $\delta^{18}O$ depletion in corals up to 10‰ to CO_2 hydration/hydroxylation. Isotopic mass balance calculation implies that $\delta^{18}O$ values of HCO_3^- produced by CO_2 hydration and hydroxylation at 19ºC are 27.5‰ and 13.8‰, respectively. The significant ^{18}O depletion of HCO_3^- relative to the equilibrium $\delta^{18}O$ values (34.3‰ at 19 ºC) indicates kinetic effects associated with CO_2 hydration/hydroxylation may indeed be a critical step leading to ^{18}O-depletion in either biological carbonates or microbially induced carbonates. In addition, Thaler et al. (2017) also proposed that the microbially induced

carbonation process, which leads to remarkable oxygen isotopic disequilibrium, may be more common in the natural system.

Two conditions favor biogenic carbonate production. The first is a confined space to facilitate the preservation of disequilibrium isotope signature (Thaler et al., 2017). A confined space may be more developed in oceanic crust with low porosity, where hydrothermal circulation is restricted (Stein and Stein, 1994). Therefore, biogenic affected DIC with ^{18}O-depletion is less likely to be diluted by seawater, and this in turn favors the precipitation of carbonate depleted in ^{18}O. The widespread low-$\delta^{18}O$ biogenic carbonates at Sites 1256D and 735B, where average porosities are remarkably low (2% to 4%), further suggest that altered oceanic crust may be an optimal place to preserve biogenic carbonate.

The second is a relatively high local pH to facilitate rapid precipitation of carbonate before oxygen isotope reaches equilibrium with ambient water (Thaler et al., 2017). The pH of water can influence (i) carbonate speciation: hydroxylation is favourable at higher pH, and thus leads to stronger ^{18}O-depletion relative to hydration as a result of the low $\delta^{18}O$ values of OH^-, which can be 38.5‰ lower than that of H_2O at 25ºC (Thornton, 1962). (ii) the rate of isotope equilibrium between DIC and water: oxygen isotopic equilibrium between DIC and water at high pH needs time orders magnitude longer than that of intermediate to low pH. For example, it requires 12h at pH = 9 and 1h at pH = 7 at 25ºC to reach O isotopic equilibrium between DIC and water (Rollion-Bard et al., 2003; Watkins et al., 2013). Relatively higher local pH can in turn lead to the short residence time of DIC. Therefore, ^{18}O-depleted carbonate is favourable when local pH is relatively high. During hydrothermal alteration of oceanic crust, pH is mainly controlled by water-rock interaction (Seyfried Jr, 1987). In the water-dominated system with high water/rock ratio of >50, the period of H^+ production is prolonged due to incorporation of

seawater Mg^{2+}, Ca^{2+}, Na^{+} into secondary minerals and leaving H^{+} in fluid, leading to a steady acidic conditions with pH around 6 (Seyfried Jr, 1987). Under rock dominated conditions, hydrolysis of silicate minerals results in the consumption of H^{+}, generating a relatively high pH environment facilitating precipitation of ^{18}O-depleted carbonates. Most importantly, similar to coral cells in which pH can be regulated by the activity of Ca-ATPase, which controls the exchange between Ca^{2+} and H^{+} and thus leads to higher pH in the calcifying fluid within cells (McConnaughey, 2003; Rollion-Bard et al., 2003), bacteria may also adjust their calcifying fluid pH and thus provide a more favourable condition for the precipitation of ^{18}O-depleted carbonates (Sumner, 2001; Visscher et al., 1998).

Besides a confined space and a relatively high local pH, biological activity in altered oceanic crust is also expected to play an essential role in the formation of biogenic carbonate. The common bio-alteration texture in altered basaltic samples indicates a deep biosphere including both autotrophic and heterotrophic bacteria (Furnes et al., 2008; Furnes and Staudigel, 1999). Autotrophic bacteria in the altered oceanic crust can supply substantial OM feeding these heterotrophic bacteria (Bach and Edwards, 2003), and the latter may utilize oxygen, sulfate or nitrate to oxidize organic matter and produce carbonate minerals (Castanier et al., 1999). Experimental studies show that carbonate minerals can precipitate during the metabolic process of sulfate-reducing bacteria (Van Lith et al., 2003). Moreover, previous studies have shown that the sulfate reduction process is able to contribute up to 50% to the OM mineralization in marine sediments (Jorgensen et al., 1992). In addition, carbonates accumulated within micritic laminae of stromatolites have long been regarded as a result of microbial process, especially sulfate-reducing process (Visscher et al., 2000; Visscher et al., 1998). So far, microbial sulfate reducing processes have been observed in low-T weathering of altered basaltic rocks and peridotite (<150

ºC) (Alford et al., 2011; Alt and Shanks, 2003, 2011), supporting an environment favoring biogenic carbonate production.

Taking into account all these factors discussed above, the strong ^{18}O depletion coupled with extremely low $\delta^{13}C_{carbonate}$ values observed in altered basalts, such as those from Site 1256D, can be best explained by an biogenic origin from heterotrophic bacteria.

Sheeted dike and gabbro samples also show large variations in $\delta^{13}C_{carbonate}$ and $\delta^{18}O_{carbonate}$ values (Fig. 4B) overlapping those of basalts (Fig. 4A). Sheeted dikes from 1256D and 504B have a $\delta^{13}C_{carbonate}$ range from -24.1‰ to 4.7‰ and a $\delta^{18}O_{carbonate}$ range from 11.4‰ to 34.0‰ (Table 1). Gabbro samples from 1256D and 735B have a $\delta^{13}C_{carbonate}$ range of -22.6‰ to 1.7‰ and a $\delta^{18}O_{carbonate}$ range from 12.5‰ to 32.3‰. A positive linear trend between $\delta^{13}C_{carbonate}$ and $\delta^{18}O_{carbonate}$ values that resembles that of altered basalts is also observed from these gabbro samples. Consistent with altered basalts, this linear trend is explained by mixing between normal marine carbonate and biogenic carbonate.

In the altered peridotites, three samples from 1271A/B show very high $\delta^{13}C_{carbonate}$ values from 6.3‰ to 10.9‰ with relatively low $\delta^{18}O_{carbonate}$ values from 12.8‰ to 22.8‰ (Fig. 4C). The high $\delta^{13}C_{carbonate}$ values can be attributed to methane formation via either high-T abiotic carbon reduction (Alt and Shanks, 2003) or low-T microbial methanogenesis (Furnes et al., 2001; Kenward et al., 2009). Both processes preferentially utilize ^{12}C and induce ^{13}C enrichment in the remaining DIC, which can be further inherited by carbonate minerals precipitated from the DIC reservoir. All the other altered peridotite samples show smaller variations in $\delta^{13}C_{carbonate}$ (-10.8‰ to 1.9‰) and $\delta^{18}O_{carbonate}$ (17.4‰ to 31.2‰) values (Fig. 4C) than those of basalts, sheeted dikes and gabbros. Yet, the $\delta^{13}C_{carbonate}$ and $\delta^{18}O_{carbonate}$ data of peridotite samples show an apparent

positive trend resembling the upper half of the data ranges of basalt, sheeted dike and gabbro. The lack of peridotite data extending close to the biogenic end-member likely reflects more efficient carbonate precipitation from seawater DIC, which results in much higher carbonate concentrations in serpentinized peridotite samples and consequently dilutes the biogenic carbonate signal.

In summary, carbonates detected in altered basalts, sheeted dikes and gabbros, and peridotite mainly originate from two common sources: normal seawater DIC and microbial affected DIC. For the normal marine carbonate, if we assume that oxygen isotopic equilibrium with seawater DIC is reached during precipitation, their $\delta^{18}O$ values (ranging from 35‰ to 25‰ in our samples; Table 1) correspond to a precipitation T of 0°C to 40°C, which is consistent with 0～60°C inferred from carbonate veins (Fig. 2). The precipitation T of biogenic carbonate is difficult to constrain due to the kinetic oxygen isotopic effect. In general, the optimum T for hyperthermophiles is less than 100°C, although some microbes can survive higher T up to 120 ºC (Kashefi and Lovley, 2003). I cannot completely rule out carbonate formation at high-T (>120ºC). However, based on the well-defined general mixing trend between normal marine carbonate and biogenic carbonate observed here, I conclude that carbonate in AOC mainly formed at low temperatures (<100°C), suggesting that the carbonates observed in gabbros and peridotite samples, existing as either normal marine carbonate or biogenic carbonate, precipitated only after these rocks were tectonically uplifted to near seafloor localities. The carbonate precipitated at high-T (>120 ºC), if there is any, should contribute little to the overall C budget in AOC. Therefore, previous studies applying the carbonate concentration of these exposed lower crustal rocks to their original depth in deeper oceanic crust, which is presumably dominated by high-T alteration, may overestimate the AOC carbon budget.

3-2 Revised AOC Carbon Input Flux

As discussed above, temperature is an important control on C uptake by AOC with most carbon precipitation in AOC at less than 60 ºC and little carbon precipitation at >100 ºC. Therefore, it is important to identify the cut-off depth of the 100 ºC isotherm, which is strongly dependent on the geothermal gradient of oceanic crust and the temperature of the sediment-basement interface, which are modeled in detail below.

(1) Oceanic Crust Thermal Gradient Estimation based on the GDH1 Plate Cooling Model

Geothermal gradient of oceanic crust as a function of crust age is strongly dependent on the heat flow of oceanic crust at different ages.

$$Q(t) = C_B \cdot \Delta T_B \quad (1)$$

in which Q (t) is the heat flow (W/m^2), C_B is the thermal conductivity ($W/m/^oK$) of oceanic crust, and ΔT_B is geothermal gradient (ºC/m) of oceanic crust.

We use a simple plate cooling model (Stein and Stein, 1992) to estimate the heat flow of oceanic crust at different ages (Fig.6**)**. The simplified equation (Stein and Stein, 1992) for the approximation of heat flow with crust aging is as follow：

$$\text{For } t \leqslant 55\text{Ma:} \qquad Q(t) = 519\, t^{-1/2} \quad (2)$$

$$\text{For } t > 55\text{Ma} \qquad Q(t) = 48 + 96 \exp(-0.0278\, t) \quad (3)$$

in which t is the crustal age. The instrumental data of the classic sites for C budget studies (e.g., DSDP/ODP/IODP sites 504B, 896A, 1256D, 396B, 801C, 417A, 417D, 843B, and 543A) all fit well with the modeling results within 10% uncertainty (Fig.6), except for Site 396B (10Ma),

which has extremely low heat flow due to the efficient hydrothermal advection. Heat flow modeled by the evolved plate cooling model (Hasterok, 2013) is also within the 10% uncertainty of heat flow data modeled by Stein and Stein (1992). The dependence of thermal conductivity with age can be determined by the variation of porosity as crust ages (see the equation by Johnson and Pruis (2003)). The results gave a thermal conductivity of 2.00 W/m/^{o}K for oceanic crust younger than 4Ma and 2.18 W/m/^{o}K for oceanic crust older than 4Ma (Johnson and Pruis, 2003)..

(2) Sediment – Basement Interface Temperature

The sediment – basement interface temperature is determined by Equation 4 below：

$$Q(t) = C_S \cdot \Delta T_S = C_S \cdot \partial T/\partial Z \quad (4)$$

in which Q (t) is the modeled heat flow by GDH1 plate model, C_S is the thermal conductivity of sediment (W/m/^{o}K), ΔT_S is the sediment geothermal gradient in ^{o}C/m, Z is the vertical dimension of sediment thickness in meters, T is the temperature in ^{o}K. The temperature at the seawater-sediment interface is labeled by the minimum carbonate vein precipitation temperature of ～0°C (Gillis and Coogan, 2011). Sediment thermal conductivity is determined by Equation 5 (Johnson and Pruis, 2003) below:

$$C_S = (8.4312 \times 10^{-4} \times Z)/2 + 1.0525 \quad (5)$$

This equation was obtained by a linear fitting on the data of global ODP sites (Johnson and Pruis, 2003). Sediment thickness (Z) is calculated by the average accumulation rate of 5.0 m

/m· y of global marine sediments (Johnson and Pruis, 2003). Therefore, the 100 ºC isotherm (D) in the basement can be determined by:

$$D = [100 - (Q(t) \times Z)/C_S]/(Q(t)/C_B) \quad (6)$$

The modeled result is shown in Fig.7. The 100 ºC isotherm varies significantly with crust age. For example, it is located at 383^{+43}_{-35} meters below the sediment-basement interface for a young oceanic crust of 1 Ma and 3222^{+358}_{-293} meters below the sediment-basement interface for an old oceanic crust of 145 Ma. The error in this estimate is mainly contributed by the 10% uncertainty of heat flow.

(3) Carbon Input Flux Estimation

In previous studies estimating the carbon budget in oceanic crust (Kelemen and Manning, 2015), the modeling employed a standard stratigraphy including several different lithologic strata (i.e., from top to bottom, 300 meters of upper volcanics, 300 meters of lower volcanics, 200 meters of transition zone, 1,200 meters of sheeted dikes, and 5,000 meters of gabbro). The C concentrations of these lithologies in the modeling were averaged results of previously published C concentration data measured on bulk samples, most of which were not measured for isotopic compositions. In our new modeling, we inherit the stratigraphic model, but consider carbon uptake only in the section less than 100 ºC. Another factor we incorporate in our model is that carbon uptake is different between young and old oceanic crust (Alt and Teagle, 1999; Coogan and Gillis, 2013; Gillis and Coogan, 2011). Because of the limited C concentration data available for global AOC samples, in order to calculate the average C concentrations of oceanic crust for further modeling of carbon input flux, we roughly divided the global oceanic crust into two age groups, younger and older than 65 Ma. 65 Ma is chosen as the division age because the

hydrothermal activity in oceanic crust decreases dramatically after 65 Ma (Mottl and Wheat, 1994; Stein and Stein, 1994).

For young AOC with age less than 65Ma, oceanic crust sections above the 100 °C isotherm mainly include upper volcanics, lower volcanics, transition, and sheeted dyke. Carbon concentration data for each section from young AOC (e.g., Sites 504B, 1256D, 896A, 597C, 411, 410, 396B, 407, 562, 556, 332A/B) were collected from literature and listed in Table 2. Weighted average carbon concentrations for young AOC upper volcanics, lower volcanics, transition zone, sheeted dike sections are further calculated by considering the drilled thickness, average dry density and average porosity of different drilling sites (Table 3).

For old AOC greater than 65Ma, the main oceanic crust sections spatially above the 100 ºC isotherm are upper volcanics, lower volcanics, transition zone, sheeted dike and upper gabbro. Table 3 lists C concentration data and calculated weighted average data for each section from old AOC (e.g., 145Ma Site 801C, 87Ma Site 543A, 106Ma Site 417A, 417D and 418A, 110Ma Site 843B, 140Ma Site 595B). I notice a dramatic C concentration increase for volcanics from young AOC to old AOC. This may be attributed to two factors. The first is a temperature effect: relatively warm bottom seawater during Cretaceous relative to the Cenozoic enhanced the water-rock interaction, which in turn lead to an increase in seawater alkalinity and thus precipitation of carbonate minerals (Coogan and Gillis, 2013; Gillis and Coogan, 2011); The second is an accumulation effect: continuous carbon uptake during low-T weathering as oceanic crust moves away from mid-ocean ridges can result in more carbonate accumulation in old altered oceanic crust (Alt and Teagle, 1999). Our limited data cannot distinguish whether the precipitation of carbonate minerals occurs over the entire life of crustal alteration or a much more focused period within ~20 Ma after the crust formed.

Applying these average C concentrations, together with the subduction rate and trench length (Jarrard, 2003), I estimate the carbon input flux from AOC for individual major subduction zones as listed in Table 4. The total global C input flux from AOC is added up as $1.3^{+0.1}_{-0.1} \times 10^{12}$ mol C/year, which is about 50 - 60% of the recent estimate by Kelemen and Manning (2015) and ~30% of the estimates by Alt and Teagle (1999) and Staudigel et al. (1989), yet still at the same order of magnitude as the seafloor sedimentary carbon from from 9×10^{11} moles/year to 5×10^{12} moles/year (Clift, 2017; Plank and Langmuir, 1998)

4. Implications

4-1 Widespread Biogenic Carbonate in AOC

According to our data, oceanic crust sections recovered by ODP/IODP 1256D and ODP 735B show obvious biogenic carbonate signals, with weighted average $\delta^{13}C$ values as low as -20.4‰ at Site 1256 (Table 5). The 10Ma DSDP Site 396B at the MAR also shows significant biogenic carbonate signals (Furnes et al., 2001), with weighted average $\delta^{13}C$ values around -6.3‰ (Table 5). The common characteristics of these altered oceanic crusts are that they are relatively young in age (<20 Ma) (Fig. 8) and relatively low in C concentrations ([C] < 1000 ppm). In contrast, the 87Ma DSDP Site 543A with higher [C] of normal marine carbonate shows no obvious biogenic carbonate signatures (Fig. 9)

If proposed above, the positive correlation between carbon and oxygen isotopes is a consequence of mixing between normal carbonate and biogenic carbonate, $\delta^{13}C$ and [C] should also show a mixing trend.

The mixing equation is derived based on the [C] and $\delta^{13}C$ values of normal marine carbonate and biogenic carbonate reservoirs. $\delta^{13}C$ value of normal marine carbonate is set as 2‰. Considering the heterogeneity of normal marine carbonate carbon concentration, [C] of this reservoir is set as a range varying from 10,000 ppm to 10 ppm (Fig. 9). $\delta^{13}C$ and [C] values of biogenic carbonate are represented by the weighted average $\delta^{13}C$ and [C] values of 1256D gabbroic rock (-20‰ and 17 ppm). These gabbroic rocks show the strongest depletions in ^{13}C and ^{18}O and are close to the biogenic carbonate end-member (Fig. 9). Based on our mixing model, when [C] of normal marine carbonate is 10,000 ppm, bulk rock $\delta^{13}C$ values range from 2‰

to 0‰ as the contribution of biogenic carbon dominated rock increases from 0% to 90% (Fig. 9). However, when [C] of normal marine carbonate is 10 ppm, bulk rock $\delta^{13}C$ values vary from 2‰ to -19‰ as the contribution of biogenic carbon dominated rock increases from 0% to 90% (Fig. 9) (see the mixing equation below). The upper 44m volcanic rocks of ODP 543A and some upper basaltic rocks in MAR samples are examples for abundant normal marine carbonate. Therefore, a biogenic carbonate signature is not shown in these altered samples even if biogenic carbonate exists. However, most of the data from ODP/IODP 1256D, ODP 735B, and 396B basalt are in accordance with mixing between normal carbonate with relatively low [C] and biogenic carbonate.

Despite the modeled mixing trend shown in Fig. 9, some data from ODP 504B, and DSDP 396B obviously sit above modeled the mixing trend, and these data have higher [C] relative to the data with similar $\delta^{13}C$ values. These outliers may mainly result from the concentration and/or isotopic heterogeneities of biogenic carbonate and/or normal carbonate reservoirs in altered oceanic crust.

Regarding the $\delta^{13}C$ and [C] distribution pattern in altered peridotite, the lack of data toward the biogenic end-member (Fig. 10) in 1271A/B, 1274A and 920D peridotite samples may be attributed to the fact that [C] of normal marine carbonate in peridotite (61ppm to 3679 ppm, with an average of 1388 ppm) is much higher than that of basalts and gabbros (11 ppm to 490 ppm, with an average of 280 ppm), thus diluting the biogenic signature.

Based on all discussion, and considering the evidence that bio-alteration and biomass production is more obvious in young AOC and shows no increasing trend in old AOC of >50Ma (Bach and Edwards, 2003; Furnes and Staudigel, 1999), we speculate that biogenic carbonate may be widespread in AOC, especially within the young ones.

4-2 A solution for the Decoupled $\delta^{13}C$ and $\delta^{15}N$ Problem in Diamonds

Diamond $\delta^{13}C$ values that deviate from the mantle range (-5±3‰) (Cartigny et al., 2014), either toward more negative ($\delta^{13}C$< -20‰) or more positive ($\delta^{13}C$>0‰) values, have been taken as direct evidence for the recycling of sedimentary organic carbon, or carbonate into at least the lithospheric mantle, or even as deep as ~700km (Palot et al., 2012; Palot et al., 2014; Tappert et al., 2005; Walter et al., 2011). Following the sedimentary recycling model, diamond formed from organic carbon should also inherit organic-like positive $\delta^{15}N$ due to the high N/C ratio of organic matter relative to mantle. However, >60% of the obviously ^{13}C-depleted diamonds do not show coupled organic-like $\delta^{13}C$ and $\delta^{15}N$ values but surprisingly show mantle-like $\delta^{15}N$ values (~-5 ± 3‰) instead, making the sedimentary carbon recycling model unsatisfactory to explain these decoupled data (Cartigny, 2005),

Previous considerations on recycled crustal carbon and nitrogen have focused on seafloor sediments. Altered oceanic crust, although a major part of subducting slabs, has not been taken into account. Our modeling shows that AOC can provide a C input flux similar to sediments. Moreover, AOC is better suited to retain its carbon during subduction through stabilizing mechanisms such as carbonate reduction (Galvez et al., 2013) and dissolution-re-carbonation (Piccoli et al., 2016). This suggests that in the deep carbon cycle AOC may act as a more important carbon reservoir than sediment. Most importantly, strong variability of $\delta^{13}C$ values in our new data makes the AOC a potential carrier of ^{13}C-depleted carbonate to diamond forming fluid. For example, weighted average $\delta^{13}C$ values of basalt, sheeted dike and gabbro at Site 1256D range from -20.4‰ to -13.0‰. ODP Site 735B, 396B, 504B have weighted average $\delta^{13}C$ values ranging from -12.0‰ to -6.3‰. Therefore, the subduction of biogenic carbonate dominated AOC, together with the secondary clay minerals, in which organic matter-like $\delta^{15}N$

ammonium is incorporated, can contribute organic-like $\delta^{13}C$ and $\delta^{15}N$ signatures to diamond forming fluids. However, carbon and nitrogen in AOC are controlled by different minerals and are thus independent from each other in both accumulation during alteration and retention during metamorphism. Therefore, AOC subducted into the deep mantle can contribute carbon and nitrogen that are decoupled with variable $(N/C)_{mantle}/(N/C)_{AOC}$ ratios and isotopic compositions. The mixing between slab-derived and mantle-derived fluids can contribute isotopically decoupled carbon and nitrogen to diamond forming fluids, and thus resolves the diamond puzzle that eclogitic diamond can have organic-like $\delta^{13}C$ values and mantle like $\delta^{15}N$ values (Fig. 11).

5. Conclusion

An investigation on combined concentration and C and O isotope measurements of carbonate in altered basalt, sheeted dike, gabbro and peridotite demonstrates that carbonates mainly consist of normal marine carbonates and biogenic carbonates, which are induced by abiotic and biological processes, respectively. More importantly, carbon uptake in the form of carbonate minerals by altered oceanic crust mainly occurs at low-T (<100 °C) alteration process at shallow depths. This discovery has two implications to our understanding of subduction-zone carbon recycling: First, the carbon budget in AOC is less than previously thought – our new estimate (1.3×10^{12} moles C per year) is only 30-60% of previous estimates. Second, biogenic carbonate with surprisingly low $\delta^{13}C$ values may be the dominant carbonate form in some oceanic crust sections, especially in young oceanic crust. Subduction of biogenic carbonate-dominated AOC, together with the ammonium in clay minerals, can explain the decoupled carbon and nitrogen isotopic pattern observed in some eclogitic diamonds.

6. Future Work

The current study has been focused on the carbonate in AOC. However, another carbon component, organic carbon, could be present in AOC but has not been studied. Organic carbon in AOC is also very important to understand the deep carbon cycle and should be a focus for future study. The understanding of organic carbon in AOC can help to address emerging scientific questions associated with several recent findings. For example, recent studies by Sverjensky et al. (2014) and Huang et al. (2017) indicate that organic carbon may play an important role in migrating carbon either in aqueous fluid or as immiscible hydrocarbon fluids under subduction zone temperature-pressure conditions. In another recent study, Plümper et al. (2017) suggests that the organic matter in serpentinite of forearc mantle may sustain a source of attractive molecules for the deep microbial communities 10,000 m below the seafloor. However, the relative organic contribution between sediment and AOC and how organic carbon behaves in sedimentary conditions vs AOC conditions in subduction zones is not fully addressed. In addition, numerous previous studies estimating the C budget in AOC relied on bulk rock data (Alt and Teagle, 1999; Kelemen and Manning, 2015; Staudigel et al., 1989), but then used it as the carbonate budget of AOC with the assumption that the organic carbon content is small in AOC. However, a comparison of our data with the bulk-carbon data by Shilobreeva et al. (2011) and Zhang et al. (2017) suggests that the organic carbon content could be higher than the carbonate carbon content at ODP/IOSP Site 1256D. This organic carbon may be absorbed by the rocks during the circulation of hydrothermal fluid, in which organic carbon comes from seawater or sediments (Loh et al., 2004), or produced in situ by abiotic or biological processes (McCarthy et al., 2011; McDermott et al., 2015). The possible high organic carbon contents in Site 1256D

imply that organic carbon may be abundant in some AOC samples, especially within the young oceanic crust, where substantial biomass may be produced (Bach and Edwards, 2003). Therefore, the role of organic carbon budget in altered oceanic crust may be underestimated by previous studies.

The constraint on the organic carbon budget in AOC can be realized by analyzing the organic carbon components in the same set of samples used in this study. We have started with DSDP 543A samples in a project collaborating with Dr. Karlis Muehlenbachs. The benefit to have a complete dataset on both carbonate and organic carbon and their isotopic compositions from the same set of AOC samples can greatly enhance our understanding of controls on carbon uptake by AOC and their impact on deep biosphere and deep carbon cycle.

Figures

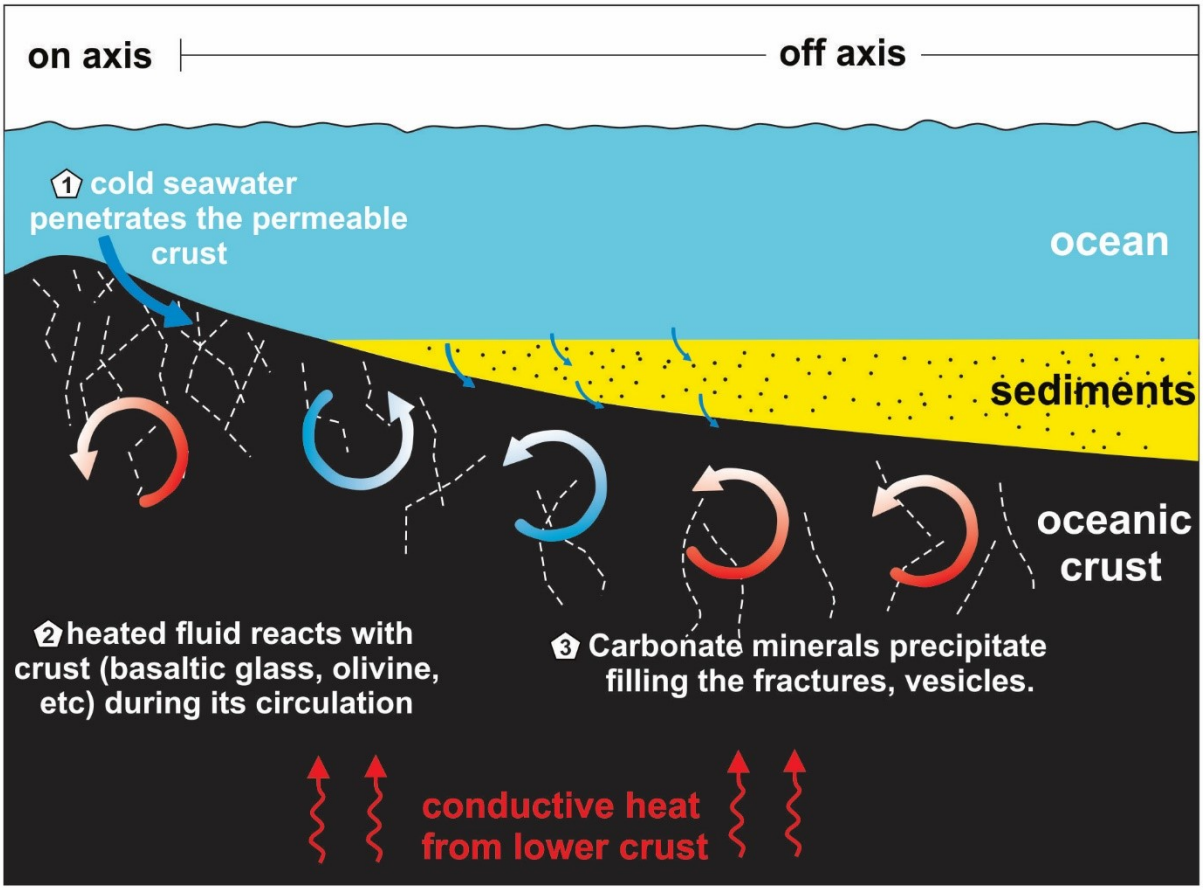

Fig.1 Hydrothermal Fluid Circulation Within Altered Oceanic Crust and Carbonate Precipitation (modified from Coggon and Teagle (2011)**).**

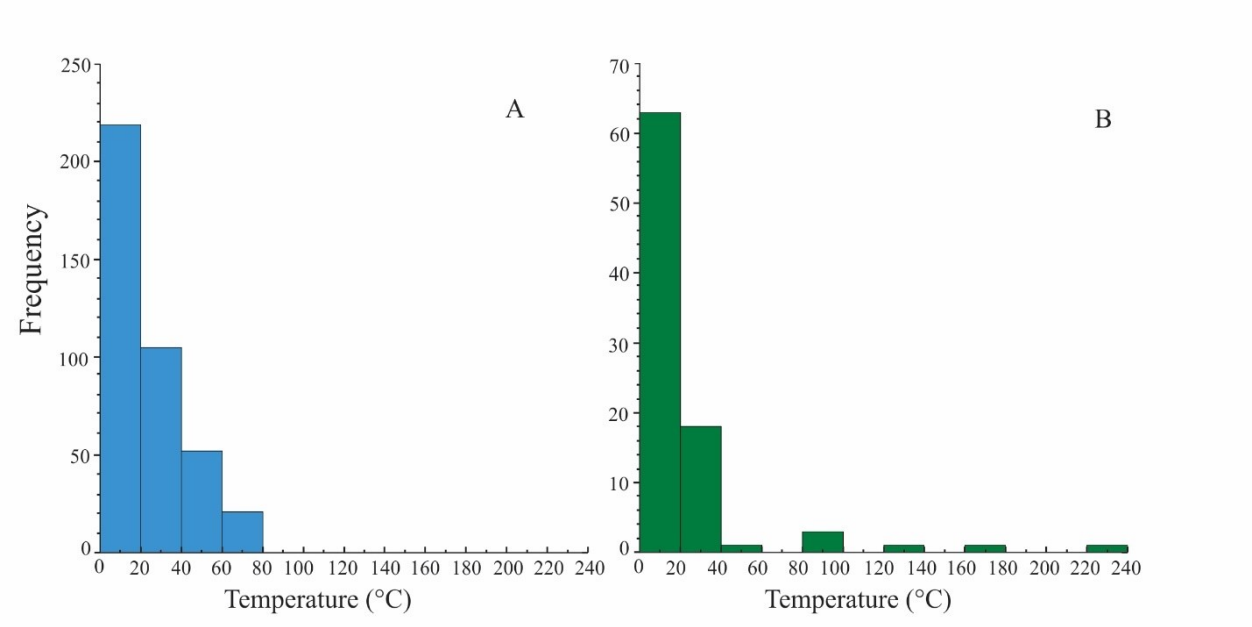

Fig.2 Histograms of precipitation temperatures of carbonate veins in basalt. Temperature was calculated using the commonly used oxygen isotope thermometry (Kim et al., 2007; O'Neil et al., 1969). (A) Carbonate veins in basalt; (B) Carbonate veins in peridotite. Data sources: (1) basalts: Alt and Teagle (2003), Böhlke et al. (1984), Gillis and Coogan (2011), Lawrence (1980), Javoy and Fouillac (1978), Muehlenbachs (1980), Hart and Staudigel (1980), Staudigel et al. (1995), Teagle et al. (1996), Coggon et al. (2006), Staudigel et al. (1986), Paul et al. (2006), Alt (1993), Coggon et al. (2010), Lawrence (1991), von Breymann and Berner (1991), Burns et al. (1990); (2) peridotite: Data sources: Schwarzenbach et al. (2013), Früh-Green et al. (2003), Agrinier et al. (1996), Bonatti et al. (1980), Bach et al. (2011), Agrinier et al. (1988), Alt and Shanks (2003), Blusztain and Hart (1996).

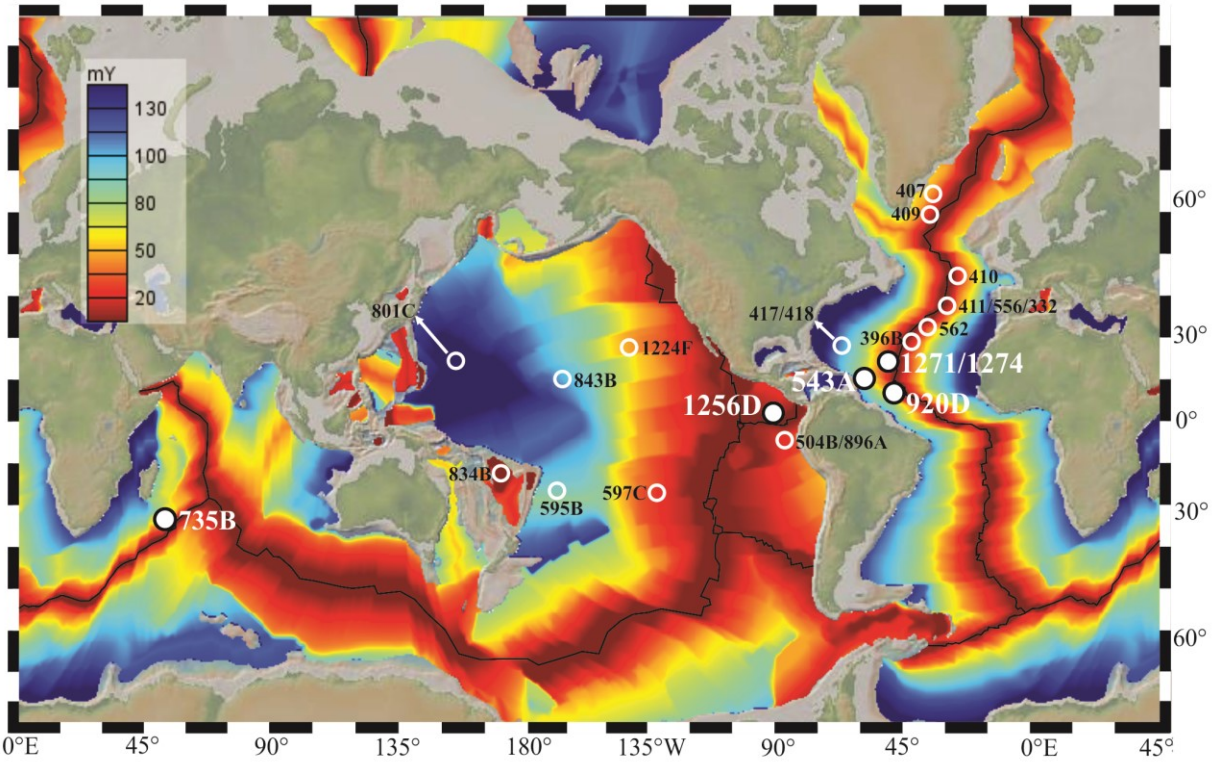

Fig.3 Sample Locations of Analyzed Samples. The crustal age map is generated by GeoMapApp (Ryan et al., 2009) (http://www.geomapapp.org) and the original oceanic crustal age grid data are from Müller et al. (2008). The DSDP/ODP/IODP samples studied here spread from the East Pacific Ocean (1256D), the Atlantic Ocean (920D, 543A, 1271/1274) and the Southwest Indian Ocean ODP Site 735B. Some other sites involved in the carbon budget estimate are also marked as white open circles for reference.

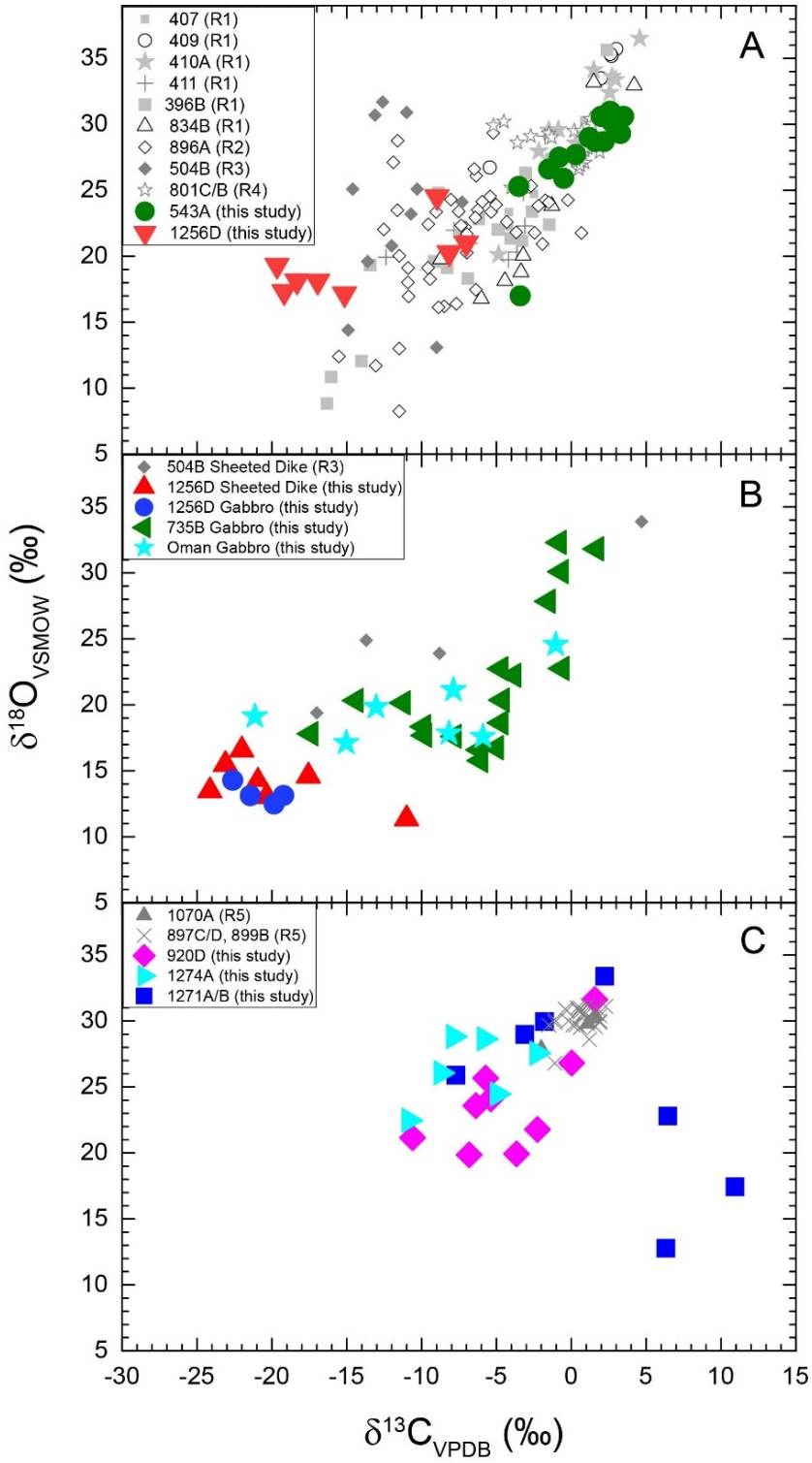

Fig.4 Bulk-rock $\delta^{13}C$ and $\delta^{18}O$ of carbonate in altered basalt, sheeted dike, gabbro, and peridotite. Data sources: R1.(Furnes et al., 2001); R2. (Torsvik et al., 1998); R3.(Furnes et al., 1999); R4.(Alt, 2003; Alt et al., 1992); R5. (Schwarzenbach et al., 2013).

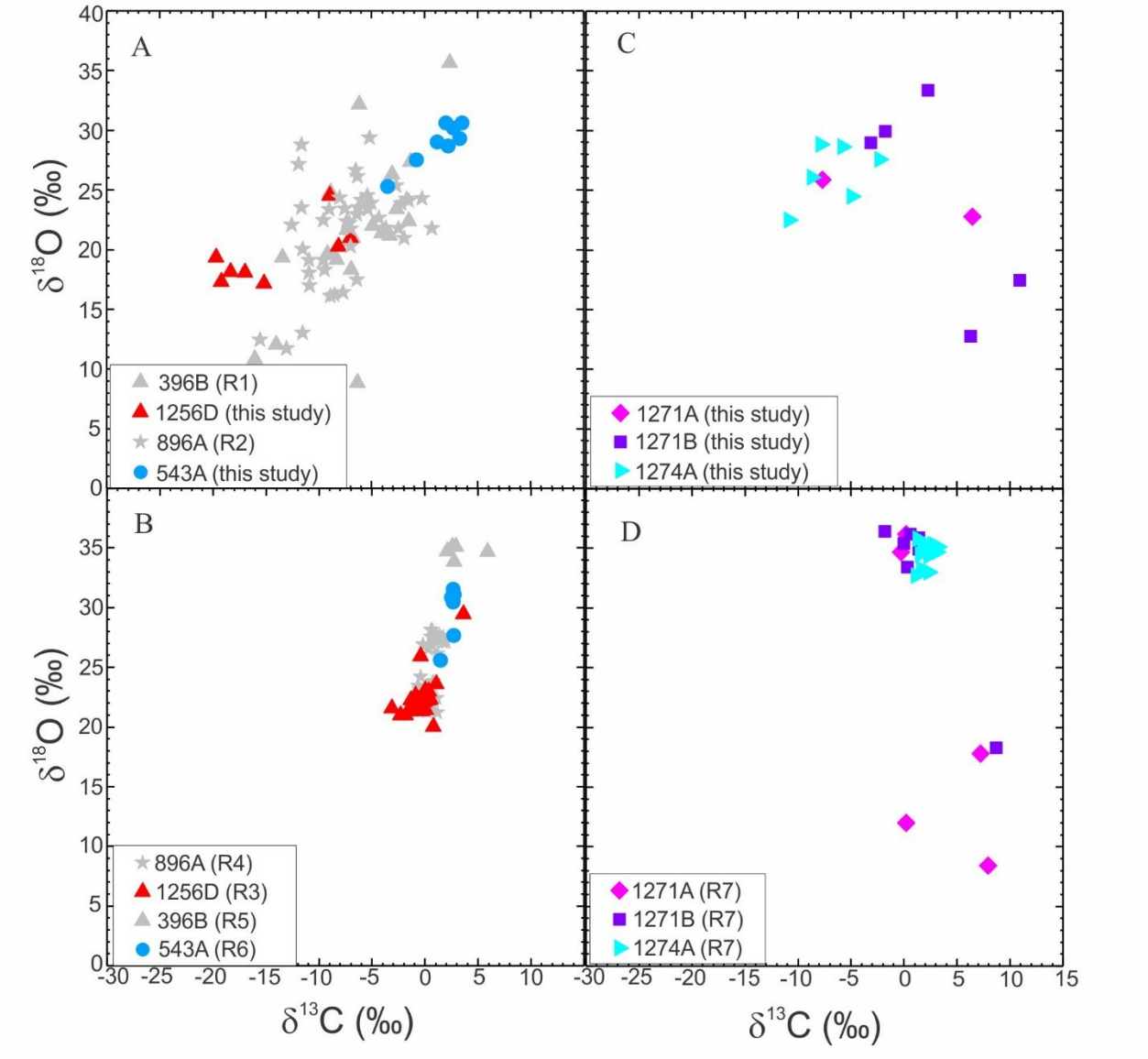

Fig.5 $\delta^{13}C_{carbonate}$ and $\delta^{18}O_{carbonate}$ Comparison Between Bulk Rock Carbonate and Carbonate Vein (bulk rock and carbonate vein data from same sites are represented by same symbol) A. Bulk rock $\delta^{18}O$ and $\delta^{13}C$ data of Basalt. B. $\delta^{18}O$ and $\delta^{13}C$ data of carbonate vein in basalt. C. Bulk rock $\delta^{18}O$ and $\delta^{13}C$ data of Peridotite. D. $\delta^{18}O$ and $\delta^{13}C$ data of carbonate vein in peridotite). Data Sources: R1. (Furnes et al., 2001) ; R2. (Torsvik et al., 1998); R3. (Coggon et al., 2006); R4. (Teagle et al., 1996); R5. (Böhlke et al., 1984); R6. (Gillis and Coogan, 2011); R7. (Bach et al., 2011). Note that the obvious decoupling of $\delta^{13}C$ and $\delta^{18}O$ values between bulk rock and carbonate vein indicates an endmember depleted in ^{13}C and ^{18}O exists in the bulk rock samples.

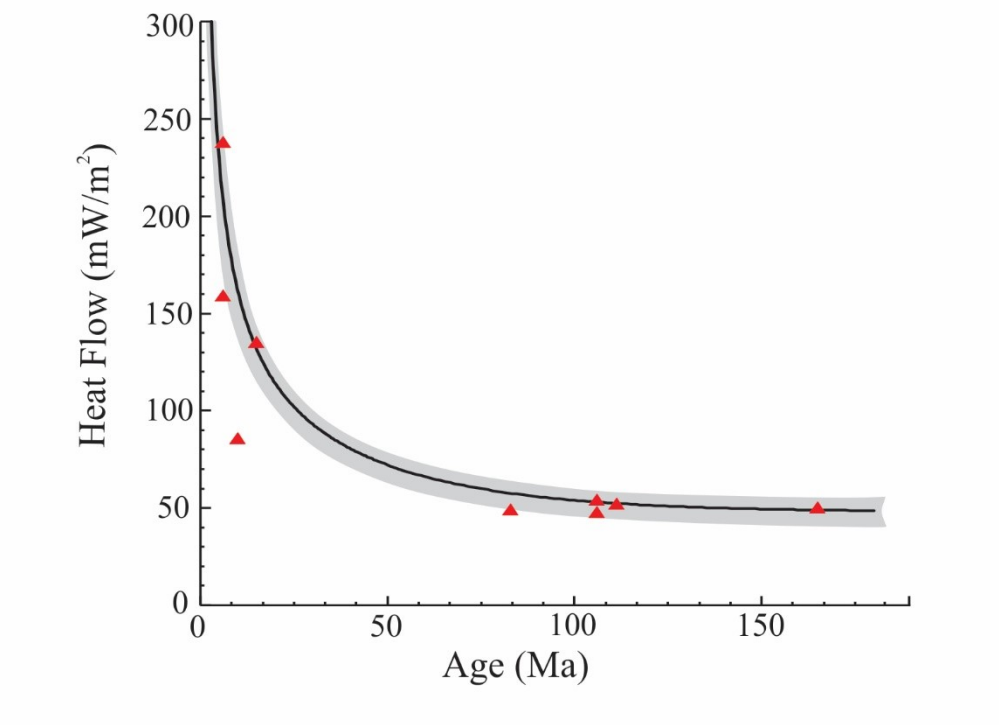

Fig.6 Comparison of heat flow from modeling results (solid curve) and instrumental data from drilling (triangles). Only the instrumental data of the classic sites for carbon budget studies are used in comparison. The instrumental data of all the sites except 396B are consistent with the modeled curve within 10% uncertainty (gray band).

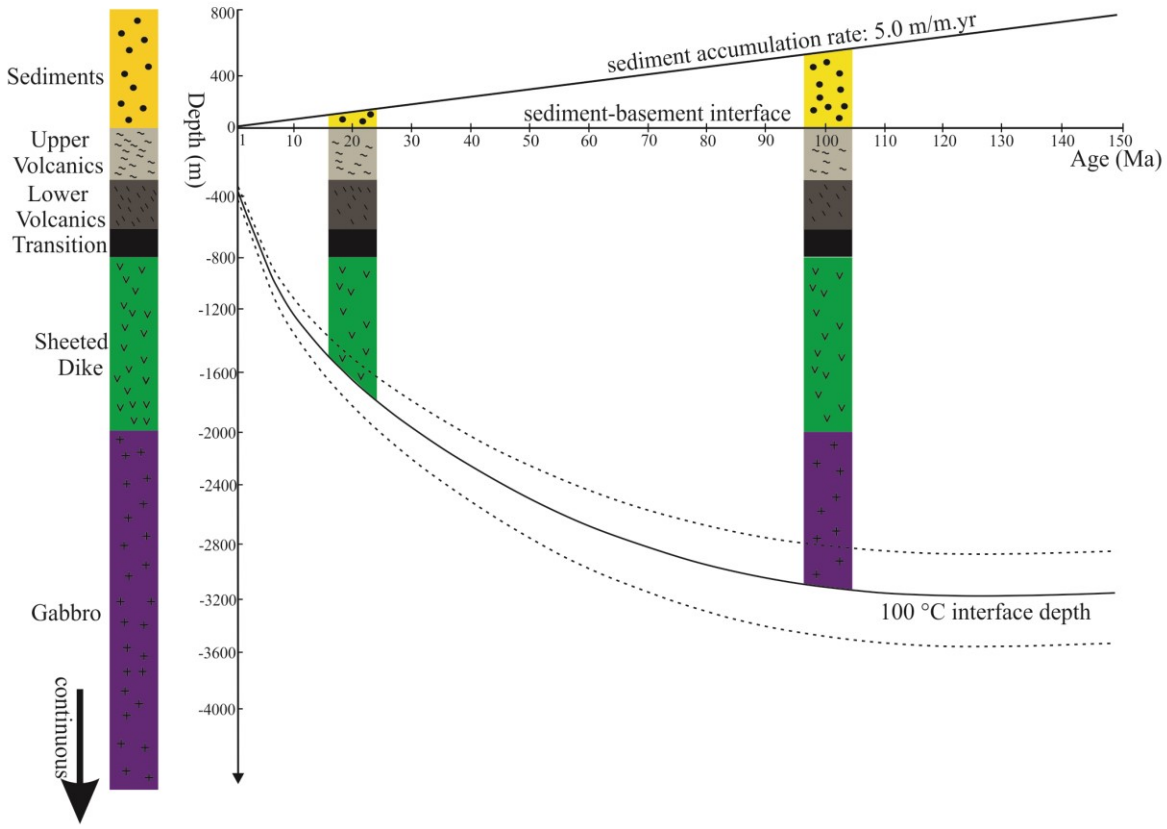

Fig.7 Along-age variations of the 100 °C isotherm in oceanic crust. See Methods for detailed explanation of modeling. A standard oceanic crust stratigraphy including overlying sediment and mafic-ultramafic oceanic crust is shown. The thickness of sediment is calculated assuming a sedimentation rate of 5 meter per million years (Johnson and Pruis, 2003). The mafic-ultramafic oceanic crust consists of 300 meters of upper volcanics, 300 meters of lower volcanics, 200 meters of transition zone, 1,200 meters of sheeted dike, and 5,000 meters of gabbro. The solid curve represents the 100°C isotherm and the dotted lines represent the uncertainty introduced mainly by the 10% error on the heat flow estimate. Two examples of oceanic crust with ages of 20 Ma and 100 Ma are shown.

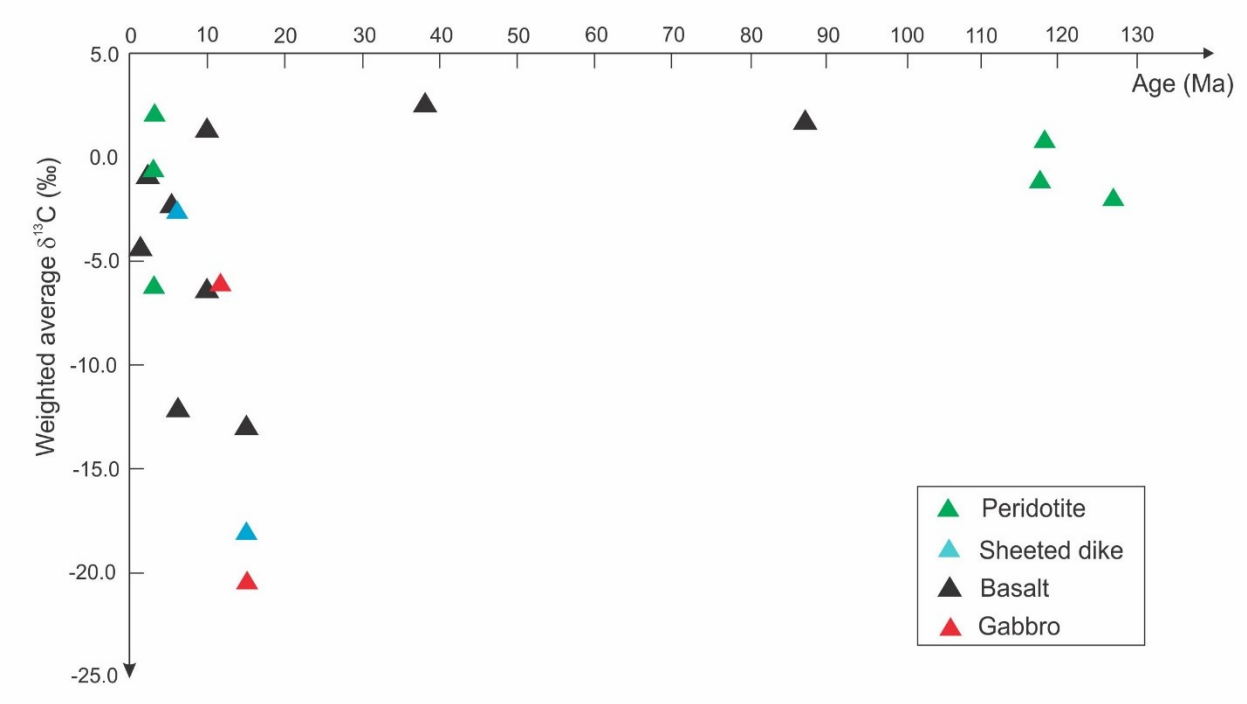

Fig.8 Along age variations of weighted average $\delta^{13}C$ (‰) in altered basalt, sheeted dike, gabbro and peridotite. Weighted average $\delta^{13}C$ values are calculated based on the density, porosity, thickness of different oceanic crust sections and are listed in Table 4. Note that biogenic carbonate signatures are only seen in young oceanic crust (< 20 Ma).

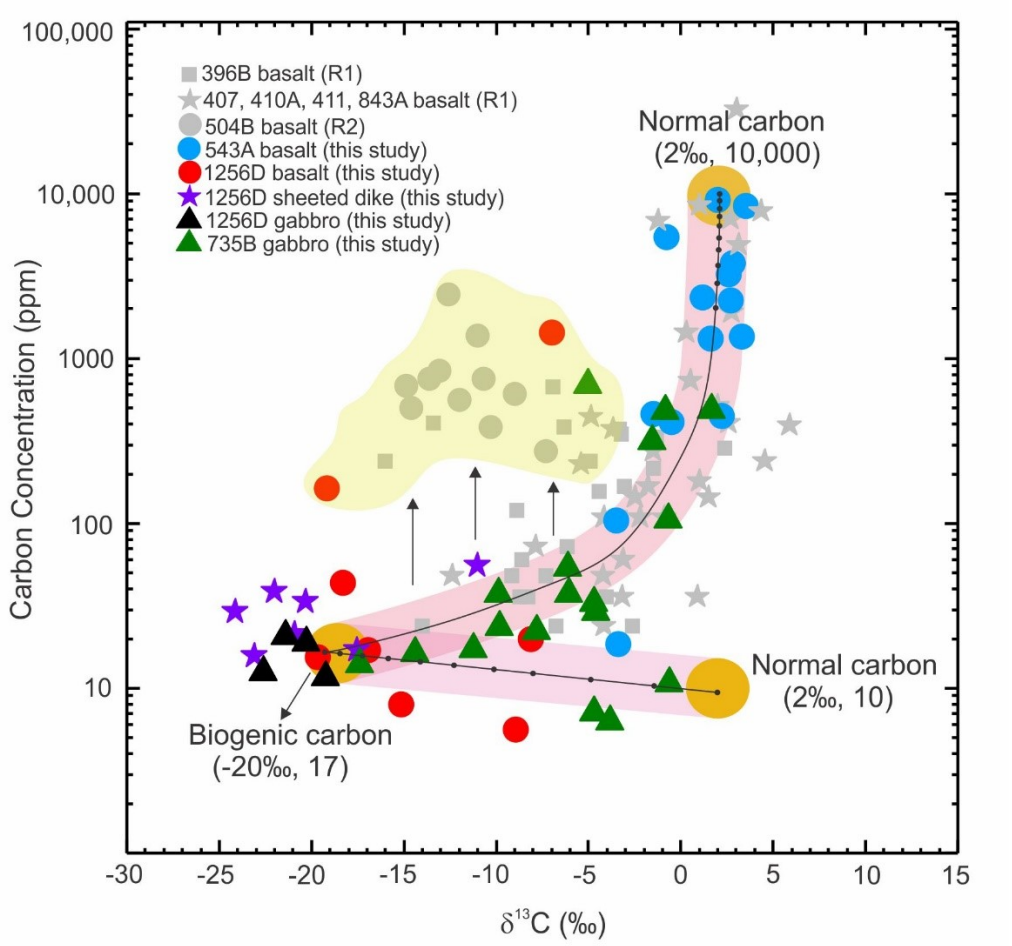

Fig.9 Carbonate Carbon Concentration ([C]) vs. $\delta^{13}C$ of Basalt, Sheeted Dike and Gabbro. Two boundary conditions are shown in the diagram. The upper boundary is the mixing line between normal marine carbonate (2‰, 10,000) and biogenic carbonate (-20‰, 17). The lower boundary is the mixing line between normal marine carbonate (2‰, 10) and biogenic carbonate (-20‰, 17). Black mixing line is derived from the equation below (see the mixing equation below in pp. 43). Filled dot along the black line is the contribution of each endmember with 10% increment. The mixing trend of upper boundary shows that bulk rock $\delta^{13}C$ varies from 2‰ to 0‰ when the contribution of biogenic carbon dominated rock increases from 0% to 90%. However, biogenic carbon contribution only increases from 0% to 1.5% due to the low [C] of biogenic carbon dominated rock. The mixing trend of lower boundary indicates that bulk rock $\delta^{13}C$ ranges from 2‰ to -19‰ when the contribution of biogenic carbon dominated rock increases from 0% to 90%. At this condition, biogenic carbon contribution increases from 0% to 94% as [C] of biogenic carbon- and normal carbon- dominated rock is comparable. Note that some data in the yellow area obviously fall outside of the mixing trend, and these data have relatively higher carbon concentration relative to the data with similar $\delta^{13}C$ values. These outlier data may mainly result from the heterogeneities of biogenic carbonate and normal marine carbonate.

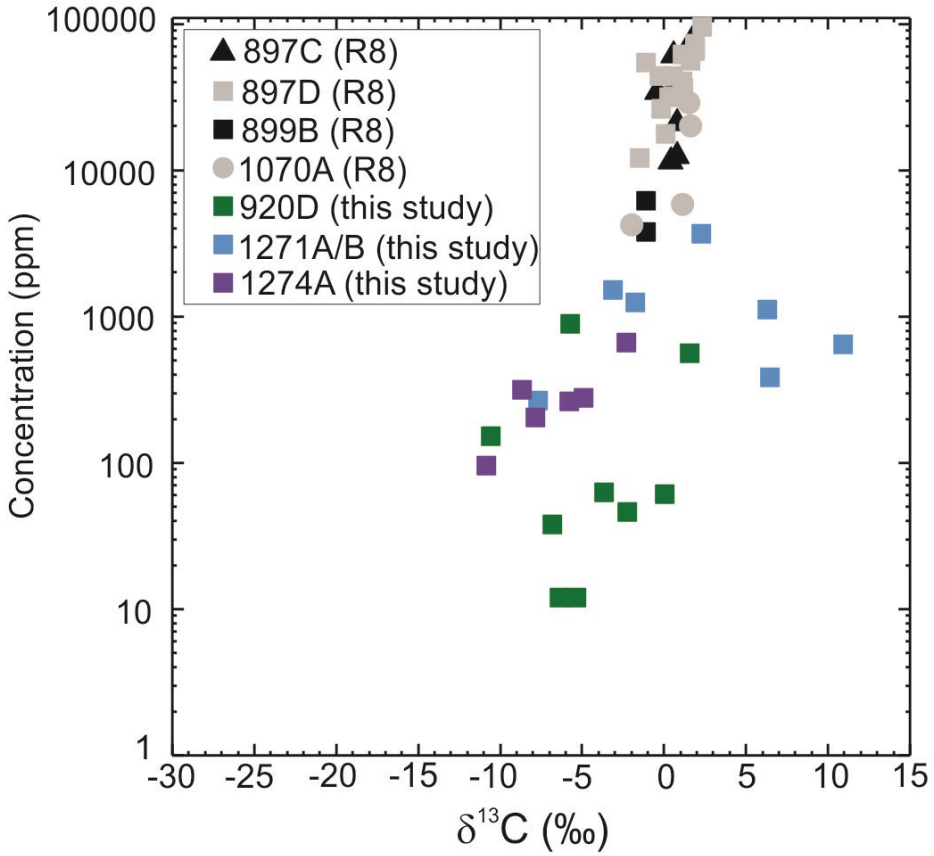

Fig.10 Relationship between $\delta^{13}C$ and Carbon Concentration ([C]) of altered Peridotite. Comparison with basalt- or gabbro host hydrothermal system (Fig. 9), overall carbon concentration is obviously higher in peridotite-host hydrothermal systems.

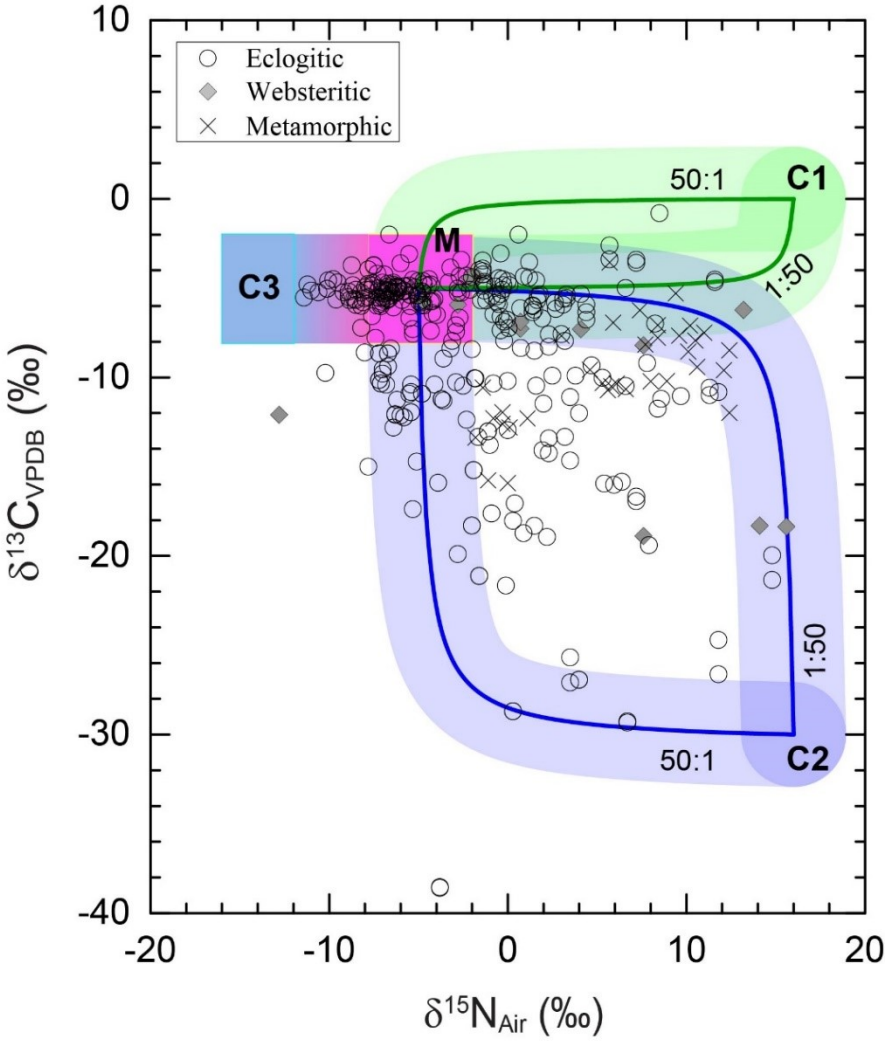

Fig. 11. Carbon versus nitrogen isotopic composition of diamonds – tracers of deep mantle carbon – along with mixing models that reflect processes leading to isotopic diversity during subduction of altered oceanic crust (AOC). Mixing models involve the mantle (M) and metamorphic equivalents of three isotopically distinct carbon and nitrogen reservoirs in AOC (C1, C2, C3). C1 = normal carbonate + low-temperature clay; C2 = biogenic carbonate (±OM) + low-temperature clay; C3 = high-temperature clay (formed by high-temperature abiotic nitrogen reduction) without crustal carbon (and thus a mantle $\delta^{13}C$ value is assigned). The shaded areas along solid curves represent mixing arrays with ±3‰ variations in $\delta^{13}C$ and $\delta^{15}N$ for each reservoir. $(N/C)_{Mantle}/(N/C)_{AOC}$ ratios for modeling are indicated along each mixing array. Note that most of the eclogitic and websteritic diamond data fall into the mixing area defined by $(N/C)_{Mantle}/(N/C)_{AOC}$ ratios from 50:1 to 1:50. Eclogitic and websteritic diamond data are from (Bulanova et al., 2014; Cartigny et al., 2009; Cartigny et al., 1999; Cartigny et al., 1998; Cartigny et al., 2004b; Laiginhas, 2008; Leost et al., 2003; Mikhail et al., 2014; Palot et al., 2012; Palot et al., 2009; Stachel et al., 2009; Thomassot et al., 2009; Van Heerden et al., 1995). Metamorphic diamonds data are from (Cartigny et al., 2004a; Cartigny et al., 2001).

Two-end Member Mixing Equations

Two end-members:

A ($\delta^{13}C_A$, $\delta^{18}O_A$), C_A (carbon concentration of A), f_1 (contribution of biogenic carbon dominated rock);

B ($\delta^{13}C_B$, $\delta^{18}O_B$), C_B (carbon concentration of B), ($1-f_1$) (contribution of normal carbonate dominated rock);

M: mixture of A and B: M ($\delta^{13}C_M$, $\delta^{18}O_M$), C_M (carbon concentration of M).

Note that f_1 is the contribution of biogenic carbon dominated rock and f_1 is different from the biogenic carbon contribution (F). The relationship between F and f_1 is:

$$F = (f_1 \times C_A)/[(f_1 \times C_A) + (1 - f_1) \times C_B] \quad (1)$$

For the two-end member mixing:

$$(^{13}C/^{12}C)_A = (\delta^{13}C_A/1000 + 1) \times R_S \ (R_S: {}^{13}C/{}^{12}C \text{ of international standard}) \quad (2)$$

$$(^{13}C/^{12}C)_B = (\delta^{13}C_B/1000 + 1) \times R_S \quad (3)$$

$$^{13}C_M = (\delta^{13}C_A/1000 + 1) \times R_S \times C_A \times f_1 + (\delta^{13}C_B/1000 + 1) \times R_S \times C_B \times (1-f_1) \quad (4)$$

$$^{12}C_M = C_A \times f_1 + C_B \times (1-f_1) \quad (5)$$

$$\delta^{13}C_M = [f_1 \times (\delta^{13}C_A \times C_A - \delta^{13}C_B \times C_B) + \delta^{13}C_B \times C_B] / [f_1 \times (C_A - C_B) + C_B] \quad (6)$$

$$\delta^{18}O_M = [f_1 \times (\delta^{18}O_A \times C_A - \delta^{18}O_B \times C_B) + \delta^{18}O_B \times C_B] / [f_1 \times (C_A - C_B) + C_B] \quad (7)$$

$$C_M = f_1 \times (C_A - C_B) + C_B \quad (8)$$

For instance, A (2‰, 32‰), B (-25‰, 18‰), C_A = 10000ppm, C_B = 24ppm, then,

$$\delta^{13}C_M = (20600 \times f_l - 600) / (9976 \times f_l + 24) \quad (9)$$

$$\delta^{18}O_M = (319568 \times f_l + 432) / (9976 \times f_l + 24) \quad (10)$$

$$C_M = 9976 \times f_l + 24 \quad (11)$$

Therefore, a straight mixing line between $\delta^{13}C_M$ and $\delta^{18}O_M$ can be plotted with f_l varying from 0 to 1 based on equation (9) and (10), and a mixing curve between $\delta^{13}C_M$ and C_M can also be plotted with f_l varying from 0 to 1 based on equation (9) and (11). These equations were derived based on Zheng and Hoefs (1993).

Tables

Table 1. Carbon and Oxygen Isotopic Composition Data of Altered Basalt, Sheeted Dike, Gabbro and Peridotite.

Location	Leg-Site	Sample Number	Depth (mbsf)	Lithology	Age (Ma)	$\delta^{13}C_{VPDB}$ (‰)	$\delta^{18}O_{VSMOW}$ (‰)	Carbonate carbon (ppm)	Reference
Atlantic	78-543A	10-01W 57-58	408	Basalt	87	2.0	30.6	9175	This study
Atlantic	78-543A	10-02W 103-105	409	Basalt	87	1.2	29.0	2351	This study
Atlantic	78-543A	10-03W 28-30	410	Basalt	87	-0.8	27.5	5464	This study
Atlantic	78-543A	11-01W 30-33	412	Basalt	87	2.2	28.7	449	This study
Atlantic	78-543A	11-02W 59-60	415	Basalt	87	3.3	29.3	1362	This study
Atlantic	78-543A	12-02W 72-75	419	Basalt	87	3.5	30.6	8382	This study
Atlantic	78-543A	12-04W 128-133	422	Basalt	87	-3.5	25.3	104	This study
Atlantic	78-543A	13-01W 18-21	425	Basalt	87	2.7	30.2	2262	This study
Atlantic	78-543A	13-05W 85-86	430	Basalt	87	1.6	18.7	1328	This study
Atlantic	78-543A	14-01W 37-39	433	Basalt	87	-3.4	17.0	19	This study
Atlantic	78-543A	15-01W 49-51	440	Basalt	87	-0.5	25.9	411	This study
Atlantic	78-543A	15-03W 99-100	442	Basalt	87	-1.5	26.6	461	This study
Atlantic	78-543A	16-01W 88-90	443	Basalt	87	2.8	30.1	3800	This study
Atlantic	78-543A	16-03W 116-118	449	Basalt	87	2.6	31.0	3263	This study
Pacific	206-1256D	2R-1 86-87	276	Basalt	15	-19.6	19.3	15	This study
Pacific	206-1256D	6R-5 99-100	300	Basalt	15	-15.1	17.2	8	This study
Pacific	206-1256D	15R-1 63-64	364	Basalt	15	-8.2	20.3	20	This study
Pacific	206-1256D	32R-2 8-9	470	Basalt	15	-9.0	24.5	6	This study
Pacific	206-1256D	65R-3 22-23	705	Basalt	15	-19.2	17.3	163	This study
Pacific	309-1256D	75R-1 112-113	752	Basalt	15	-7.0	21.0	1444	This study

Location	Leg-Site	Sample Number	Depth (mbsf)	Lithology	Age (Ma)	$\delta^{13}C_{VPDB}$(‰)	$\delta^{18}O_{VSMOW}$ (‰)	Carbonate carbon (ppm)	Reference
Pacific	309-1256D	92R-1 95-96	869	Basalt	15	-18.3	18.1	43	This study
Pacific	309-1256D	100R-1 133-134	910	Basalt	15	-16.9	18.1	17	This study
Atlantic	49-407	37-1 112-113	339.6	Basalt	38	1.03	28.73	180	1
Atlantic	49-407	39-1 52-53	358	Basalt	38	-2.48	24.73	144	1
Atlantic	49-407	41-1 2-3	376.5	Basalt	38	-4.17	22.27	24	1
Atlantic	49-407	42-2 58-59	388.1	Basalt	38	-4.17	23.35	108	1
Atlantic	49-407	45-3 93-95	437.4	Basalt	38	0.88	30.32	36	1
Atlantic	49-409	21-1 3-4	205.1	Basalt	2.5	1.98	33.5	516	1
Atlantic	49-409	21-1 32-33	214.8	Basalt	2.5	3.01	35.7	32292	1
Atlantic	49-409	25-2 40-41	244.9	Basalt	2.5	2.7	35.19	7020	1
Atlantic	49-409	25-3 36-37	266.4	Basalt	2.5	2.61	35.33	408	1
Atlantic	49-409	32-1 60-61	310.1	Basalt	2.5	-5.43	26.73	228	1
Atlantic	49-410A	2-1 3-4	334.5	Basalt	10	2.56	32.4	8232	1
Atlantic	49-410A	2-1 53-54	335	Basalt	10	4.56	36.51	240	1
Atlantic	49-410A	2-2 50-51	336.5	Basalt	10	-0.87	29.61	108	1
Atlantic	49-410A	2-3 50-51	338	Basalt	10	-1.5	29.55	276	1
Atlantic	49-410A	2-5 96-97	341.5	Basalt	10	2.97	33.39	5196	1
Atlantic	49-410A	3-1 113-114	345.1	Basalt	10	0.54	27.42	732	1
Atlantic	49-410A	3-4 6-7	348.6	Basalt	10	0.3	28.56	1440	1
Atlantic	49-410A	4-1 134-135	354.8	Basalt	10	-2.17	27.96	108	1

Location	Leg-Site	Sample Number	Depth (mbsf)	Lithology	Age (Ma)	$\delta^{13}C_{VPDB}$ (‰)	$\delta^{18}O_{VSMOW}$ (‰)	Carbonate carbon (ppm)	Reference
Atlantic	49-410A	4-1 140-141	354.9	Basalt	10	1.51	34.12	144	1
Atlantic	49-410A	6-1 86-87	373.4	Basalt	10	-4.85	20.13	444	1
Atlantic	49-410A	6-2 125-126	375.31	Basalt	10	2.73	33.63	1908	1
Atlantic	49-411	1-1 40-41	74.4	Basalt	1	-3.1	22.31	60	1
Atlantic	49-411	2-1 4-5	81.5	Basalt	1	-3.64	20.33	372	1
Atlantic	49-411	2-1 4-5	81.5	Basalt	1	-4.91	19.73	48	1
Atlantic	49-411	2-1 7-8	81.6	Basalt	1	-1.75	29.11	168	1
Atlantic	49-411	2-2 21-22	83.2	Basalt	1	-7.83	21.99	72	1
Atlantic	49-411	2-2 21-22	83.2	Basalt	1	-12.37	19.93	48	1
Atlantic	49-411	3-1 94-95	91.9	Basalt	1	-3.2	24.8	36	1
Atlantic	46-396B	4-1 87-88	151.4	Basalt	10	-6.77	20.99	24	1
Atlantic	46-396B	5-1 136-137	158.9	Basalt	10	-14.01	12.05	24	1
Atlantic	46-396B	7-1 10-11	174.1	Basalt	10	-8.29	19.13	36	1
Atlantic	46-396B	7-2 93-94	176.4	Basalt	10	-8.87	24.81	120	1
Atlantic	46-396B	8-2 5-6	186.1	Basalt	10	-7.33	21.66	48	1
Atlantic	46-396B	9-1 128-129	194.3	Basalt	10	-8.6	19.59	60	1
Atlantic	46-396B	10-1 56-57	203.1	Basalt	10	-6.91	18.32	672	1
Atlantic	46-396B	10-2 14-15	204.2	Basalt	10	-9.16	19.62	48	1
Atlantic	46-396B	11-1 89-90	212.9	Basalt	10	-16.31	8.84	384	1
Atlantic	46-396B	14-1 8-9	225.6	Basalt	10	-6.18	23.17	72	1

Location	Leg-Site	Sample Number	Depth (mbsf)	Lithology	Age (Ma)	$\delta^{13}C_{VPDB}$(‰)	$\delta^{18}O_{VSMOW}$ (‰)	Carbonate carbon (ppm)	Reference
Atlantic	46-396B	17-2 26-27	269.3	Basalt	10	-1.34	27.36	336	1
Atlantic	46-396B	17-3 64-65	271.2	Basalt	10	-16.02	10.84	240	1
Atlantic	46-396B	17-3 109-110	271.6	Basalt	10	-4.05	21.36	36	1
Atlantic	46-396B	17-4 54-55	272.6	Basalt	10	-1.47	22.39	216	1
Atlantic	46-396B	20-1 135-136	287.9	Basalt	10	2.4	35.64	288	1
Atlantic	46-396B	20-4 114-115	292.2	Basalt	10	-2.63	23.39	24	1
Atlantic	46-396B	20-5 72-73	293.3	Basalt	10	-3.06	26.31	168	1
Atlantic	46-396B	21-2 44-45	298	Basalt	10	-3.29	21.18	108	1
Atlantic	46-396B	21-2 44-45	298	Basalt	10	-13.43	19.34	408	1
Atlantic	46-396B	23-1 92-93	316	Basalt	10	-4.9	22.02	240	1
Pacific	135-834B	14R-1 28-29	165	Basalt	5.5	-3.35	18.79	372	1
Pacific	135-834B	14R-1 39-40	166.1	Basalt	5.5	1.5	33.19	8100	1
Pacific	135-834B	15R-1 53-55	175.9	Basalt	5.5	4.21	32.95	7776	1
Pacific	135-834B	15-2 35-36	177.2	Basalt	5.5	-3.21	20.06	348	1
Pacific	135-834B	16R-1 40-41	183.4	Basalt	5.5	-4.44	18.14	156	1
Pacific	135-834B	18-1 8-9	204.1	Basalt	5.5	-1.29	23.82	6936	1
Pacific	135-834B	33R-1 6-7	281.3	Basalt	5.5	-6.01	16.79	396	1
Pacific	135-834B	35R-1 32-33	291.1	Basalt	5.5	-8.71	19.79	36	1
Pacific	148-896A	2R-1 47-49	201.31	Basalt	6	-5.95	24.14	n.d	2
Pacific	148-896A	5R-2 39-41	229.7	Basalt	6	-2.45	21.78	n.d	2

Location	Leg-Site	Sample Number	Depth (mbsf)	Lithology	Age (Ma)	$\delta^{13}C_{VPDB}$(‰)	$\delta^{18}O_{VSMOW}$ (‰)	Carbonate carbon (ppm)	Reference
Pacific	148-896A	6R-2 39-45	239.77	Basalt	6	-11.49	20.04	n.d	2
Pacific	148-896A	6R-2 39-45	239.77	Basalt	6	-11.48	8.25	n.d	2
Pacific	148-896A	6R-3 30-34	241.08	Basalt	6	-8.49	16.21	n.d	2
Pacific	148-896A	7R-1 58-60	247.98	Basalt	6	-1.73	24.24	n.d	2
Pacific	148-896A	9R-1 17-21	266.87	Basalt	6	-5.36	23.36	n.d	2
Pacific	148-896A	9R-1 17-21	266.87	Basalt	6	-11.89	27.12	n.d	2
Pacific	148-896A	9R-1 90-92	267.6	Basalt	6	-9.56	19.12	n.d	2
Pacific	148-896A	9R-1 90-92	267.6	Basalt	6	-6.37	17.46	n.d	2
Pacific	148-896A	9R-1 125-130	267.95	Basalt	6	-11.61	23.49	n.d	2
Pacific	148-896A	9R-1 125-130	267.95	Basalt	6	-9.43	18.28	n.d	2
Pacific	148-896A	10R-1 40-46	276.8	Basalt	6	-9.02	23.37	n.d	2
Pacific	148-896A	10R-1 40-46	276.8	Basalt	6	-4.31	22.62	n.d	2
Pacific	148-896A	11R-1 0-3	286	Basalt	6	-13.05	11.71	n.d	2
Pacific	148-896A	11R-1 0-3	286	Basalt	6	-0.22	24.27	n.d	2
Pacific	148-896A	11R-1 73-75	286.73	Basalt	6	-8.87	16.13	n.d	2
Pacific	148-896A	11R-1 73-75	286.73	Basalt	6	-7.68	16.41	n.d	2
Pacific	148-896A	11R-1 111-113	287.11	Basalt	6	-6.25	23.52	n.d	2
Pacific	148-896A	11R-1 111-113	287.11	Basalt	6	-9.55	22.43	n.d	2
Pacific	148-896A	12R-2 7-9	297.14	Basalt	6	-2.19	23.83	n.d	2
Pacific	148-896A	12R-1 76-80	315.36	Basalt	6	-6.35	26.1	n.d	2

Location	Leg-Site	Sample Number	Depth (mbsf)	Lithology	Age (Ma)	$\delta^{13}C_{VPDB}$(‰)	$\delta^{18}O_{VSMOW}$ (‰)	Carbonate carbon (ppm)	Reference
Pacific	148-896A	12R-1 76-80	315.36	Basalt	6	-15.52	12.41	n.d	2
Pacific	148-896A	14R-2 28-30	316.29	Basalt	6	-6.48	26.63	n.d	2
Pacific	148-896A	14R-2 58-60	316.59	Basalt	6	0.67	21.77	n.d	2
Pacific	148-896A	14R-2 111-112	317.14	Basalt	6	-5.42	24.54	n.d	2
Pacific	148-896A	16R-1 31-32	334.21	Basalt	6	-6.4	22.94	n.d	2
Pacific	148-896A	16R-3 89-91	337.58	Basalt	6	-2.69	25.35	n.d	2
Pacific	148-896A	17R-3 11-15	346.55	Basalt	6	-1.93	20.93	n.d	2
Pacific	148-896A	17R-3 11-15	346.55	Basalt	6	-11.49	13.00	n.d	2
Pacific	148-896A	18R-1 75-77	353.82	Basalt	6	-7.52	23.4	n.d	2
Pacific	148-896A	21R-3 25-27	376.2	Basalt	6	-5.21	29.35	n.d	2
Pacific	148-896A	22R-4 31-33	287.33	Basalt	6	-3.68	21.82	n.d	2
Pacific	148-896A	24R-1 18-19	402.01	Basalt	6	-1.5	24.08	n.d	2
Pacific	148-896A	25R-2 130-132	414.03	Basalt	6	-8.04	24.31	n.d	2
Pacific	148-896A	26R-3 43-46	424.29	Basalt	6	-6.97	20.28	n.d	2
Pacific	148-896A	26R-3 43-46	424.29	Basalt	6	-7.11	22.19	n.d	2
Pacific	148-896A	27R-1 114-117	431.64	Basalt	6	-10.9	19.12	n.d	2
Pacific	148-896A	27R-1 1414-117	431.64	Basalt	6	-10.92	18.02	n.d	2
Pacific	148-896A	27R-1 108-111	433.04	Basalt	6	-11.59	28.77	n.d	2
Pacific	148-896A	28R-1 23-26	440.23	Basalt	6	-12.51	22.04	n.d	2
Pacific	148-896A	28R-1 23-26	440.23	Basalt	6	-10.87	16.96	n.d	2

Location	Leg-Site	Sample Number	Depth (mbsf)	Lithology	Age (Ma)	$\delta^{13}C_{VPDB}$(‰)	$\delta^{18}O_{VSMOW}$ (‰)	Carbonate carbon (ppm)	Reference
Pacific	148-896A	29R-2 4-6	451.13	Basalt	6	-7.36	22.34	n.d	2
Pacific	148-896A	30R-1 61-63	459.91	Basalt	6	-5.03	23.91	n.d	2
Pacific	148-896A	30R-1 61-63	459.91	Basalt	6	-6.97	21.7	n.d	2
Pacific	69-504B	4-5 91-92	286.92	Basalt	6	-9	13.1	612	3
Pacific	69-504B	21-4 90-92	426.42	Basalt	6	-7.3	24.1	276	3
Pacific	69-504B	21-4 90-92	426.42	Basalt	6	-10.3	25.1	384	3
Pacific	69-504B	24-3 73-94	451.93	Basalt	6	-14.9	14.4	684	3
Pacific	69-504B	24-3 73-94	451.93	Basalt	6	-12	20.8	564	3
Pacific	69-504B	28-4 16-17	479.67	Basalt	6	-13.6	19.6	756	3
Pacific	70-504B	35-1 109-111	535.61	Basalt	6	-10.7	23.2	756	3
Pacific	70-504B	48-2 123-124	649.74	Basalt	6	-13.1	30.7	840	3
Pacific	70-504B	48-2 123-124	649.74	Basalt	6	-14.6	25.1	504	3
Pacific	70-504B	62-2 23-25	756.75	Basalt	6	-12.6	31.7	2460	3
Pacific	70-504B	64-1 27-28	773.28	Basalt	6	-11	30.9	1380	3
Pacific	129-801C	\	\	Composite	145	-2.7	29.1	n.d	4
Pacific	129-801C	\	\	Composite	145	0.2	29.5	n.d	4
Pacific	129-801C	\	\	Composite	145	-1.5	29.3	n.d	4
Pacific	129-801C	\	\	Composite	145	0.9	28.2	n.d	4
Pacific	129-801C	\	\	Composite	145	0.9	28	n.d	4
Pacific	129-801C	\	\	Composite	145	0.9	28.3	n.d	4

Location	Leg-Site	Sample Number	Depth (mbsf)	Lithology	Age (Ma)	$\delta^{13}C_{VPDB}$(‰)	$\delta^{18}O_{VSMOW}$ (‰)	Carbonate carbon (ppm)	Reference
Pacific	129-801C	\	\	Composite	145	1.1	29.1	n.d	4
Pacific	129-801C	\	\	Composite	145	-0.2	27.5	n.d	4
Pacific	129-801C	\	\	Composite	145	0	27.8	n.d	4
Pacific	129-801C	\	\	Composite	145	0.5	26.6	n.d	4
Pacific	129-801C	\	\	Composite	145	0.9	27.1	n.d	4
Pacific	129-801C	\	\	Composite	145	0.6	26.9	n.d	4
Pacific	129-801C	\	\	Composite	145	0.7	27.9	n.d	4
Pacific	129-801B	40R-1 85-91	477.75	Basalt	145	-3.6	28.6	n.d	5
Pacific	129-801B	41R-1 26-31	483.26	Basalt	145	-5.2	29.9	n.d	5
Pacific	129-801B	41R-1 88-94	483.88	Basalt	145	-4.5	30.2	n.d	5
Pacific	129-801B	43R-2 21-27	493.78	Basalt	145	-1.3	29	n.d	5
Pacific	129-801C	5R-1 103-105	532.23	Basalt	145	1.9	27.9	n.d	5
Pacific	129-801C	R-2 87-89	533.33	Basalt	145	0.3	27.3	n.d	5
Pacific	129-801C	5R-3 38-43	534.15	Basalt	145	0.7	29.5	n.d	5
Pacific	129-801C	5R-3 125-131	535.02	Basalt	145	1.3	30.4	n.d	5
Pacific	129-801C	5R-3 125-131	535.02	Basalt	145	1.4	30	n.d	5
Pacific	129-801C	8R-1 65-67	560.15	Basalt	145	1.1	28.2	n.d	5
Pacific	129-801C	8R-2 78-80	561.03	Basalt	145	0.3	27.7	n.d	5
Pacific	309-1256D	130R-2 49-50	1065	Sheeted Dike	15	-23.1	15.5	16	This study
Pacific	309-1256D	136R-1 74-75	1094	Sheeted Dike	15	-11.0	11.4	56	This study

Location	Leg-Site	Sample Number	Depth (mbsf)	Lithology	Age (Ma)	$\delta^{13}C_{VPDB}$ (‰)	$\delta^{18}O_{VSMOW}$ (‰)	Carbonate carbon (ppm)	Reference
Pacific	309-1256D	169R-3 53-54	1247	Sheeted Dike	15	-22.0	16.6	38	This study
Pacific	312-1256D	173R-1 12-13	1255	Sheeted Dike	15	-24.1	13.5	29	This study
Pacific	312-1256D	181R-1 63-64	1290	Sheeted Dike	15	-20.3	13.1	34	This study
Pacific	312-1256D	189R-1 70-71	1300	Sheeted Dike	15	-17.5	14.6	17	This study
Pacific	312-1256D	196R-1 35-36	1362	Sheeted Dike	15	-20.9	14.2	21	This study
Pacific	140-504B	208R-1 30-32	1778.32	Sheeted Dike	6	-13.7	24.9	492	3
Pacific	140-504B	213R-1 45-47	1812.97	Sheeted Dike	6	-17	19.4	504	3
Pacific	140-504B	222R-1 2-4	1884.64	Sheeted Dike	6	-8.8	23.9	1104	3
Pacific	140-504B	245B-1 36-38	2043.18	Sheeted Dike	6	4.7	33.9	23856	3
Pacific	312-1256D	214R-2 101-102	1364	Gabbro	15	-19.2	13.1	12	This study
Pacific	312-1256D	223R-3 24-25	1449	Gabbro	15	-19.8	12.5	19	This study
Pacific	312-1256D	230R-2 45-46	1483	Gabbro	15	-21.4	13.1	21	This study
Pacific	312-1256D	234R-1 30-31	1501	Gabbro	15	-22.6	14.3	12	This study
Indian	118-735B	1D-1-10W 69-73	0.73	Gabbro	11.5	-4.7	22.7	7.1	This study
Indian	118-735B	7D-1-10W 70-73	26.7	Gabbro	11.5	-11.2	20.2	17.3	This study
Indian	118-735B	10D-2-2bW 17-21	37.7	Gabbro	11.5	-0.8	32.3	479.2	This study
Indian	118-735B	16R-5-1cW 40-43	66.8	Gabbro	11.5	-0.7	30.1	105.4	This study
Indian	118-735B	23R-2-1bW 29-32	101.4	Gabbro	11.5	-4.6	20.4	29.0	This study
Indian	118-735B	37R-1-2bW 22-25	176.2	Gabbro	11.5	-3.9	22.2	6.2	This study
Indian	118-735B	52R-4-4aW 60-61	252.3	Gabbro	11.5	-0.6	22.8	10.7	This study

Location	Leg-Site	Sample Number	Depth (mbsf)	Lithology	Age (Ma)	$\delta^{13}C_{VPDB}$(‰)	$\delta^{18}O_{VSMOW}$ (‰)	Carbonate carbon (ppm)	Reference
Indian	118-735B	69R-3-5cW 82-85	343.8	Gabbro	11.5	-14.4	20.3	16.3	This study
Indian	118-735B	80R-6-2W 16-17	430.9	Gabbro	11.5	-4.7	18.6	33.1	This study
Indian	176-735B	90R-1-2W 105-107	508.8	Gabbro	11.5	-17.4	17.8	14.1	This study
Indian	176-735B	95R-1-7W 105-109	545.7	Gabbro	11.5	1.7	31.8	489.9	This study
Indian	176-735B	108R-2-1cW 36-37	625.3	Gabbro	11.5	-7.8	17.6	22.4	This study
Indian	176-735B	122R-2-1bW 11-15	730.8	Gabbro	11.5	-1.6	27.9	314.4	This study
Indian	176-735B	130R-4-8bW 116-119	799.3	Gabbro	11.5	-6.1	15.8	37.3	This study
Indian	176-735B	138R-3-1W 61-64	864.6	Gabbro	11.5	-9.8	17.7	23.4	This study
Indian	176-735B	149R-7-2W 18-121	968.7	Gabbro	11.5	-9.9	18.4	37.4	This study
Indian	176-735B	180R-5-4W 38-40	1236.7	Gabbro	11.5	-5.0	16.7	693.0	This study
Indian	176-735B	200R-4-1bW 37-38	1406.5	Gabbro	11.5	-6.1	16.6	53.6	This study
Oman	\	G2-1	\	Gabbro	94	-5.9	17.6	50.3	This study
Oman	\	G4-1	\	Gabbro	94	-13.0	19.8	29.6	This study
Oman	\	G6-1	\	Gabbro	94	-7.9	21.1	13.8	This study
Oman	\	G5-1	\	Gabbro	94	-8.2	17.8	25.1	This study
Oman	\	G3-1	\	Gabbro	94	-21.1	19.1	101.8	This study
Oman	\	G7-1	\	Gabbro	94	-1.0	24.6	43.5	This study
Oman	\	G1-1	\	Gabbro	94	-15.0	17.1	13.7	This study
Atlantic	153-920D	2R-1 37-40	8.4	Peridotite	<1	1.6	31.6	559	This study
Atlantic	153-920D	5R-4 12-13	40.9	Peridotite	<1	-6.4	23.6	12	This study
Atlantic	153-920D	8R-1 118-119	67.1	Peridotite	<1	-5.4	24.1	12	This study
Atlantic	153-920D	10R-3 74-75	81.7	Peridotite	<1	-6.8	19.9	38	This study

Location	Leg-Site	Sample Number	Depth (mbsf)	Lithology	Age (Ma)	$\delta^{13}C_{VPDB}$(‰)	$\delta^{18}O_{VSMOW}$ (‰)	Carbonate carbon (ppm)	Reference
Atlantic	153-920D	12R-5 37-38	100.9	Peridotite	<1	-5.7	25.7	893	This study
Atlantic	153-920D	16R-7 42-45	141.4	Peridotite	<1	-2.3	21.8	46	This study
Atlantic	153-920D	19R-2 15-17	163.8	Peridotite	<1	0.0	26.8	61	This study
Atlantic	153-920D	20R-2 28-31	173.3	Peridotite	<1	-3.6	19.9	63	This study
Atlantic	153-920D	22R-2 75-78	192.6	Peridotite	<1	-10.6	21.2	153	This study
Atlantic	209-1271A	1R-1 44-45	0.4	Peridotite	<3	6.4	22.8	382	This study
Atlantic	209-1271A	4R-2 74-77	30.5	Peridotite	<3	-7.7	25.9	267	This study
Atlantic	209-1271B	5R-1 48-50	28.2	Peridotite	<3	-3.1	29.0	1529	This study
Atlantic	209-1271B	7R-1 56-58	36.8	Peridotite	<3	10.9	17.4	645	This study
Atlantic	209-1271B	10R-1 102-104	51.5	Peridotite	<3	2.2	33.4	3679	This study
Atlantic	209-1271B	12R-1 112-115	61.2	Peridotite	<3	6.3	12.8	1112	This study
Atlantic	209-1271B	19R-2 18-21	95.8	Peridotite	<3	-1.8	30.0	1254	This study
Atlantic	209-1274A	2R-1 19-22	12.1	Peridotite	<3	-2.3	27.6	667	This study
Atlantic	209-1274A	6R-1 43-45	31.2	Peridotite	<3	-10.8	22.5	96	This study
Atlantic	209-1274A	11R-1 38-41	55.3	Peridotite	<3	-4.9	24.5	279	This study
Atlantic	209-1274A	16R-2 61-63	85.8	Peridotite	<3	-7.9	28.8	205	This study
Atlantic	209-1274A	20R-1 51-54	103.4	Peridotite	<3	-8.7	26.1	314	This study
Atlantic	209-1274A	25R-1 40-43	136.9	Peridotite	<3	-5.8	28.6	262	This study
Iberian	149-897C	\	650.77	Peridotite	118	-0.4	30.9	34380	6
Iberian	149-897C	\	661.17	Peridotite	118	0.8	30.6	12410	6
Iberian	149-897C	\	661.72	Peridotite	118	0.4	31	11450	6
Iberian	149-897C	\	662.49	Peridotite	118	0.6	30.7	61400	6

Location	Leg-Site	Sample Number	Depth (mbsf)	Lithology	Age (Ma)	$\delta^{13}C_{VPDB}$ (‰)	$\delta^{18}O_{VSMOW}$ (‰)	Carbonate carbon (ppm)	Reference
Iberian	149-897D	\	686.37	Peridotite	118	0.1	29.7	17710	6
Iberian	149-897D	\	698.65	Peridotite	118	1.1	31.2	61960	6
Iberian	149-897D	\	707.75	Peridotite	118	2.3	31.1	96150	6
Iberian	149-897D	\	713.85	Peridotite	118	0.5	30.8	44370	6
Iberian	149-897D	\	718.92	Peridotite	118	0.6	29.5	32060	6
Iberian	149-897D	\	743.11	Peridotite	118	-0.3	30.8	44140	6
Iberian	149-897D	\	743.38	Peridotite	118	-1.5	29.7	12080	6
Iberian	149-897D	\	743.96	Peridotite	118	-0.2	30.0	26330	6
Iberian	149-897D	\	748.52	Peridotite	118	1.9	30.4	65450	6
Iberian	149-897D	\	751.93	Peridotite	118	1.9	30.0	67490	6
Iberian	149-897D	\	752.02	Peridotite	118	1.9	29.9	72910	6
Iberian	149-897D	\	753.5	Peridotite	118	1.6	29.6	56100	6
Iberian	149-897D	\	754.8	Peridotite	118	1.2	28.6	36100	6
Iberian	149-897D	\	756.37	Peridotite	118	1.1	29.8	40850	6
Iberian	149-897D	\	757.33	Peridotite	118	0.3	29.7	31420	6
Iberian	149-897D	\	758.4	Peridotite	118	-1.1	29.9	54860	6
Iberian	149-899B	\	512.01	Peridotite	118	-1.1	30.1	6150	6
Iberian	149-899B	\	548.58	Peridotite	118	-1.1	26.8	3770	6
Iberian	173-1070A	\	667.69	Peridotite	127	1.1	29.8	5860	6
Iberian	173-1070A	\	668.91	Peridotite	127	1.6	30.4	20100	6
Iberian	173-1070A	\	669.86	Peridotite	127	1.5	30.2	29020	6
Iberian	173-1070A	\	696.36	Peridotite	127	-2.0	27.9	4210	6

Data sources:

1.Furnes et al. (2001); 2. Torsvik et al. (1998); 3.Furnes et al. (1999); 4.Alt (2003); 5. Alt (1993); 6.Schwarzenbach et al. (2013).

Table 2. Carbon Concentrations of Young AOC

Site	Age (Ma)	Bulk carbon concentration (ppm)	Drilled depth (m)	Average dry density (g/cm^3)	Average porosity (%)	Reference
Upper Volcanics						
504B	6	573	300	2.90	6.00	7,8
1256D	15	416	284	2.82	3.60	9,10
896A	6	1391	290	2.94	4.60	7,11
597C	28	1091	90	3.06	5.90	12,13,14
411	1	115†	46	2.95	6.00	15,16
410A	10	1712†	52	2.60	6.00	15,17
396B	10	2182	256	2.86	5.56	12,18
407	38	99†	177	2.83	6.00	15,19
562	17	5182	90	2.82	4.00	12,20
556	30	5455	177	2.77	8.40	12,21
1224F	48	1364	147	2.77	6.80	12,22
409	2.5	2043†	150	2.60	6.00	15,25
834B	5.5	3015†	128	2.90	6.00	15,26
332A	3.5	600	331	2.96	8.14	23
332B	3.5	2018	583	2.93	7.10	23
Weighted average		1645				

Table 2 Continued

Sites	Age (Ma)	Bulk carbon concentration (ppm)	Drilled depth (m)	Average dry density (g/cm^3)	Average porosity (%)	References
Lower Volcanics						
504B	6	382	300	3	5	7,8
1256D	15	366	720	2.9	3.2	9,10
Weighted average		371				
Transition						
504B	6	1581	200	2.9	3	7,24
1256D	15	511	60	2.9	3	9,10
Weighted average		1334				
Sheeted Dike						
504B	6	191	1200	2.97	1.7	7,24
1256D	15	358	350	3.01	1.5	9,24
Weighted average		229				
Weighted average of young AOC		a*				

† Bulk carbon concentration is not available for AOC. The carbonate is isotopically characterized by a "normal carbonate" signature and the carbonate concentrations are very high. Organic carbon is generally minor compared to carbonate in such reservoirs. Thus, the carbonate carbon concentrations are used to represent the bulk carbon concentration.

* Weighted average carbon concentration (a) for young AOC is calculated based on a 7,000-meter thick oceanic crust but with carbon only in the topmost strata spatially above the 100 ºC isotherm (i.e., for oceanic crust with age of 6 Ma, 300 meters of upper volcanics,

300 meters of lower volcanics, 200 meters of transition zone, and 185 meters of upper sheeted dikes are included) and their corresponding weighted average carbon concentrations, average densities, average porosities of each strata. Applying the weighted average carbon concentration of young AOC, together with trench length and subduction rate, carbon input fluxes of individual subduction zones with young AOC subducting can be calculated and listed in Table 4.

Data Sources: 7.Alt and Teagle (1999); 8.Shipboard Scientific Party. (1993a); 9.Shilobreeva et al. (2011); 10.Shipboard Scientific Party. (2003a); 11.Shipboard Scientific Party. (1993b); 12.Gillis and Coogan (2011); 13.Shipboard Scientific Party. (1986); 14.Jörg Erzinger. (1986); 15.Furnes et al. (2001); 16.Shipboard Scientific Party. (1979b); 17.Shipboard Scientific Party. (1979a); 18. Drummond Matthews. (1979); 19.Chroston et al. (1979); 20.Shipboard Scientific Party. (1985b); 21.Shipboard Scientific Party. (1985a); 22.Shipboard Scientific Party. (2003b); 23.Shipboard scientific Party. (1977); 24.Expedition 309/312 Scientists. (2006).

Table 3. Carbon Concentrations of old AOC

Sites	Age (Ma)	Bulk carbon concentration (ppm)	Drilled depth (m)	Average dry density (g/cm^3)	Average porosity (%)	References
Upper Volcanics						
801C	145	5435	300	2.83	9	7,25
417A	106	10655	209	2.8	3.4	26, 27
417D	106	11318	365	2.73	3.7	26, 27
418A	106	10909	300	2.75	3.5	12, 27
843B	110	6545	69	2.7	6	7,28
543A	87	5727	44	2.88	6.4	29
595B	140	5182	54	2.8	4	12
Weighted average		9157				
Lower Volcanics						
418A	120	2304	244	2.9	3	26, 27
801C	165	2359	159	2.86	7.9	7,13
Weighted average		2325				
Transition	\	1334*	\	\	\	7,9
Sheeted dike	\	229*	\	\	\	7,9
Gabbro	\	391‡	\	\	\	9
Weighted average of old AOC		b★				

* Carbon concentration data of old AOC transition, sheeted dike and gabbro section are not available. The weighted average carbon concentrations of transition zone and sheeted dike sections of young AOC (Table 2) are used here.

‡ Carbon concentration of gabbro section of old AOC is represented by the average carbon concentration of gabbro at site 1256D (Shilobreeva et al., 2011; Zhang et al., 2017).

★ Weighted average carbon concentration (b) for old AOC is calculated based on a 7,000-meter oceanic crust but with carbon only in the topmost strata spatially above the 100 ºC isotherm (i.e., for oceanic crust with age of 145 Ma, 300 meters of upper volcanics, 300 meters of lower volcanics, 200 meters of transition zone, 1,200 meters of sheeted dikes, and 1222 meters of gabbros are included) and their corresponding weighted average carbon concentrations, average densities, average porosities of each strata. Applying the weighted average carbon concentration of old AOC, together with trench length and subduction rate, carbon input fluxes of individual subduction zones with old AOC subducting can be calculated and listed in Table 4.

Data Sources: 7.Alt and Teagle (1999); 25.Shipboard Scientific Party. (1990); 26.Staudigel et al. (1989); 27.Christensen et al. (1980); 28.Shipboard Scientific Party. (1992); 29.Shipboard Scientific Party. (1984); 12.Gillis and Coogan (2011); 13.Shipboard Scientific Party. (2000); 9.Shilobreeva et al. (2011).

Table 4. Carbon input fluxes of world's major subduction zones.

Trench	Age (Ma)	Length (km)	Subduction rate (meters/year)	Carbon input flux (moles/year)
Young AOC				
Alaska	49	1490	0.056	2.4E+10
Aleutian, E	56	1246	0.059	2.3E+10
C. America	16	1506	0.072	2.5E+10
Cascadia	5	990	0.036	6.9E+09
Chile, C	23	1306	0.074	2.4E+10
Chile, N	41	1579	0.074	3.3E+10
Chile, S	16	1218	0.016	4.5E+09
Colombia	21	1355	0.065	2.1E+10
Cotabato	42	500	0.02	2.9E+09
Manlia	30	1050	0.01	2.7E+09
Mexico	9	1383	0.049	1.4E+10
Nankai	23	824	0.038	7.6E+09
Negros	16	400	0.02	1.8E+09
New Britain	50	600	0.11	2.0E+10
Peru	37	1599	0.065	2.9E+10
Philippine	43	1509	0.064	2.8E+10
Ryukyu	46	1153	0.057	1.8E+10
San Cristobal	50	1050	0.049	1.6E+10
Scotia	57	1005	0.044	1.4E+10
Sulawesi, N.	42	600	0.03	5.2E+09
Sulu	16	500	0.02	2.3E+09
Sumatra	61	2462	0.05	4.0E+10
Trobriand	50	590	0.02	3.6E+09
Vanuatu	40	1189	0.111	3.7E+10
Yep-Palau	32	550	0.003	4.3E+08
Total				4.0E+11

Table 4. Continued

Old AOC				
Aegean	90	850	0.005	4.1E+09
Aleutian, W	72	1102	0.018	1.9E+10
Andaman	83	1089	0.023	2.4E+10
Lesser Antilles, N	87	400	0.024	9.1E+09
Lesser Antilles, S	87	400	0.024	9.1E+09
Hikurangi	100	794	0.021	1.6E+10
Izu-Bonin	145	1167	0.05	5.6E+10
Japan, NE	132	1061	0.076	7.8E+10
Java	100	1200	0.071	8.2E+10
Kamchatka	115	900	0.074	6.4E+10
Kermadec	100	1422	0.052	7.1E+10
Kurile	128	1243	0.075	9.0E+10
Markan	97	950	0.037	3.4E+10
Sunda, E	145	950	0.071	6.5E+10
Mariana	134	1812	0.047	8.2E+10
Tonga	100	1460	0.148	2.1E+11
Total				9.1E+11
Global Total		44454		1.3E+12

Table 5. Weighted average $\delta^{13}C$, $\delta^{18}O$ and carbon concentration of DSDP, ODP, IODP oceanic sections.

Site	Lithology	$\delta^{13}C$（Weighted Average）	$\delta^{18}O$（Weighted Average)	Reference
1256D	Basalt	-13.0	19.7	this study
543A	Basalt	1.8	28.7	this study
396B	Basalt	-6.3	23.8	1
407	Basalt	-0.6	27.1	1
409	Basalt	2.6	35.2	1
410A	Basalt	1.4	31.0	1
411	Basalt	-4.3	21.9	1
834B	Basalt	-2.3	22.8	1
504B	Basalt	-12.0	25.5	3
504B	Sheeted Dike	-2.5	28.6	3
1256D	Sheeted Dike	-18.0	14.4	this study
735B	Gabbro	-6.0	19.5	this study
1256D	Gabbro	-20.4	13.2	this study
1271A	Peridotite	-0.5	24.3	this study
1274A	Peridotite	-6.1	26.1	this study
1271B	Peridotite	2.1	23.1	this study
897C	Peridotite	0.9	30.7	6
897D	Peridotite	0.9	30.5	6
899B	Peridotite	-1.2	28.9	6
1070A	Peridotite	-1.9	29.2	6

References

Agrinier, P. and Cannat, M. (1997) Oxygen isotope constraints on serpentinization processes in ultramafic rocks from the Mid-Atlantic Ridge (23°N). *In* Karson, J.A., Cannat, M., Miller, D.J., and Elthon, D. (Eds.) ,, *Proc. ODP, Sci. Results*, 153: College Station, TX (Ocean Drilling Program), 381–388.

Agrinier, P., Cornen, G. and Beslier, M.-O. (1996) Mineralogical and oxygen isotopic features of serpentinites recovered from the ocean/continent transition in the Iberia Abyssal Plain. *In* Whitmarsh, R.B., Sawyer, D.S., Klaus, A., and Masson, D.G. (Eds.), *Proc. ODP, Sci. Results*, 149: College Station, TX (Ocean Drilling Program), 541-552. 10.2973/odp.proc.sr.149.223.1996.

Agrinier, P., Mével, C. and Girardeau, J. (1988) Hydrothermal alteration of the peridotites cored at the ocean/continent boundary of the Iberian margin: petrologic and stable isotope evidence. *In* Boillot, G., Winterer, EL, et al, *Proc. ODP, Sci. Results*, 103: College Station, TX (Ocean Drilling Program), 225-234.

Alford, S.E., Alt, J.C. and Shanks, W.C. (2011) Sulfur geochemistry and microbial sulfate reduction during low-temperature alteration of uplifted lower oceanic crust: insights from ODP Hole 735B. Chem. Geol. 286, 185-195.

Alt, J. (1993) Low-temperature alteration of basalts from the Hawaiian Arch, Leg 136. *In* Wilkens, R.H., Firth, J.V., Bender, J., et al, *Proc. ODP, Init. Repts*, 136: College Station, TX (Ocean Drilling Program), 133-146. 10.2973/odp.proc.sr.136.214.1993.

Alt, J.C. (2003) Stable isotopic composition of upper oceanic crust formed at a fast spreading ridge, ODP Site 801. Geochem. Geophys. Geosyst. 4.

Alt, J.C. and Bach, W. (2001) Data Report: low-grade hydrothermal alteration of uplifted lower oceanic crust, Hole 735B: Mineralogy and Isotope Geochemistry, Proceedings of the Ocean Drilling Program, Scientific Results. Vol. 176, pp. 1-24., pp. 1-24.

Alt, J.C., France-Lanord, C., Floyd, P.A., Castillo, P. and and Galy, A. (1992) Low-temperature hydrothermal alteration of Jurassic ocean crust, Site 801. In Larson, R.L., Lancelot, Y., et al.,. Proc. ODP, Sci. Results, 129: College Station, TX (Ocean Drilling Program), 415–427.

Alt, J.C., Laverne, C., Coggon, R.M., Teagle, D.A., Banerjee, N.R., Morgan, S., Smith‐Duque, C.E., Harris, M. and Galli, L. (2010) Subsurface structure of a submarine hydrothermal system in ocean crust formed at the East Pacific Rise, ODP/IODP Site 1256. Geochemistry, Geophysics, Geosystems 11.

Alt, J.C. and Shanks, W.C. (2003) Serpentinization of abyssal peridotites from the MARK area, Mid-Atlantic Ridge: sulfur geochemistry and reaction modeling. Geochim. Cosmochim. Acta. 67, 641-653.

Alt, J.C. and Shanks, W.C. (2011) Microbial sulfate reduction and the sulfur budget for a complete section of altered oceanic basalts, IODP Hole 1256D (eastern Pacific). Earth and Planetary Science Letters 310, 73-83.

Alt, J.C., Shanks, W.C., Bach, W., Paulick, H., Garrido, C.J. and Beaudoin, G. (2007) Hydrothermal alteration and microbial sulfate reduction in peridotite and gabbro exposed by detachment faulting at the Mid‐Atlantic Ridge, 15° 20′ N (ODP Leg 209): A sulfur and oxygen isotope study. Geochemistry, Geophysics, Geosystems 8.

Alt, J.C. and Teagle, D.A. (1999) The uptake of carbon during alteration of ocean crust. Geochim. Cosmochim. Acta. 63, 1527-1535.

Alt, J.C. and Teagle, D.A. (2003) Hydrothermal alteration of upper oceanic crust formed at a fast-spreading ridge: mineral, chemical, and isotopic evidence from ODP Site 801. Chem. Geol. 201, 191-211.

Bach, W. and Edwards, K.J. (2003) Iron and sulfide oxidation within the basaltic ocean crust: implications for chemolithoautotrophic microbial biomass production. Geochim. Cosmochim. Acta. 67, 3871-3887.

Bach, W., Rosner, M., Jöns, N., Rausch, S., Robinson, L.F., Paulick, H. and Erzinger, J. (2011) Carbonate veins trace seawater circulation during exhumation and uplift of mantle rock: results from ODP Leg 209. Earth Planet. Sci. Lett. 311, 242-252.

Blusztain, J. and Hart, S.R. (1996) Sr and O isotopic ratios of aragonite veins from Site 895. *In* Mével, C., Gillis, K.M., Allan, J.F., and Meyer, P.S, *Proc. ODP, Sci. Results*, 147: College Station, TX (Ocean Drilling Program), 311-313. 10.2973/odp.proc.sr.147.035.1996.

Böhlke, J., Alt, J. and Muehlenbachs, K. (1984) Oxygen isotope–water relations in altered deep-sea basalts: low-temperature mineralogical controls. Can. J. Earth Sci. 21, 67-77.

Bonatti, E. (1976) Serpentinite protrusions in the oceanic crust. Earth Planet Sci. Lett. 32, 107-113.

Bonatti, E., Lawrence, J., Hamlyn, P. and Breger, D. (1980) Aragonite from deep sea ultramafic rocks. Geochim. Cosmochim. Acta 44, 1207-1214.

Brady, P.V. and Gíslason, S.R. (1997) Seafloor weathering controls on atmospheric CO 2 and global climate. Geochim. Cosmochim. Acta. 61, 965-973.

Bulanova, G., de Vries, D.W., Pearson, D., Beard, A., Mikhail, S., Smelov, A. and Davies, G. (2014) An eclogitic diamond from Mir pipe (Yakutia), recording two growth events from different isotopic sources. Chem. Geol. 381, 40-54.

Burns, S.J., Swart, P.K. and Baker, P.A. (1990) Geochemistry of Secondary Carbonates in Leg 115 Basalts: Tracers of Basalt/Seawater Interaction. *In* Duncan, R.A., Backman, J., Peterson, L.C., et al, *Proc. ODP, Sci. Results*, 115 College Station, TX (Ocean Drilling Program), 93-101. 10.2973/odp.proc.sr.115.183.1990.

Cannat, M. (1996) How thick is the magmatic crust at slow spreading oceanic ridges? J. Geophys. Res. Solid Earth 101, 2847-2857.

Cannat, M., Bideau, D. and Bougault, H. (1992) Serpentinized peridotites and gabbros in the Mid-Atlantic Ridge axial valley at 15 37′ N and 16 52′ N. Earth Planet Sci. Lett. 109, 87-106.

Cannat, M., Mevel, C., Maia, M., Deplus, C., Durand, C., Gente, P., Agrinier, P., Belarouchi, A., Dubuisson, G. and Humler, E. (1995) Thin crust, ultramafic exposures, and rugged faulting patterns at the Mid-Atlantic Ridge (22–24 N). Geology 23, 49-52.

Cartigny, P. (2005) Stable isotopes and the origin of diamond. Elements 1, 79-84.

Cartigny, P., Chinn, I., Viljoen, K.F. and Robinson, D. (2004a) Early Proterozoic ultrahigh pressure metamorphism: evidence from microdiamonds. Science 304, 853-855.

Cartigny, P., De Corte, K., Shatsky, V.S., Ader, M., De Paepe, P., Sobolev, N.V. and Javoy, M. (2001) The origin and formation of metamorphic microdiamonds from the Kokchetav massif, Kazakhstan: a nitrogen and carbon isotopic study. Chem. Geol. 176, 265-281.

Cartigny, P., Farquhar, J., Thomassot, E., Harris, J.W., Wing, B., Masterson, A., McKeegan, K. and Stachel, T. (2009) A mantle origin for Paleoarchean peridotitic diamonds from the Panda kimberlite, Slave Craton: evidence from ^{13}C-, ^{15}N-and ^{33,34} S-stable isotope systematics. Lithos 112, 852-864.

Cartigny, P., Harris, J. and Javoy, M. (1999) Eclogitic, peridotitic and metamorphic diamonds and the problems of carbon recycling—the case of Orapa (Botswana), The JB Dawson Volume—Proceedings of the Seventh International Kimberlite Conference, Cape Town. Red Roof Design, Cape Town, pp. 117-124.

Cartigny, P., Harris, J.W. and Javoy, M. (1998) Eclogitic diamond formation at Jwaneng: No room for a recycled component. Science 280, 1421-1424.

Cartigny, P., Palot, M., Thomassot, E. and Harris, J.W. (2014) Diamond formation: A stable isotope perspective. Annu. Rev. Earth Planet. Sci. 42, 699-732.

Cartigny, P., Stachel, T., Harris, J.W. and Javoy, M. (2004b) Constraining diamond metasomatic growth using C-and N-stable isotopes: examples from Namibia. Lithos 77, 359-373.

Castanier, S., Le Métayer-Levrel, G. and Perthuisot, J.-P. (1999) Ca-carbonates precipitation and limestone genesis—the microbiogeologist point of view. Sediment. Geol. 126, 9-23.

Christensen, N.I., Blair, S.C., Wilkens, R.H. and Salisbury, M.H. (1980) Compressional wave velocities, densities, and porosities of basalts from Holes 417A, 417D, adn 418A, Deep Sea Drilling Project Leg 51-53. *In* Donnelly, T., Francheteau, J., Bryan, W., Robinson, P., Flower, M.,Salisbury, M., et al, *Init. Repts. DSDP*, 51, 52, 53: Part 2:Washington (U.S. Government Printing Office), 1467-1471. 10.2973/dsdp.proc.515253.167.1980.

Chroston, P.N., Evans, C.J. and Lee, C. (1979) Laboratory measurements of compressional wave velocities and electrical resistivity of basalts from DSDP Leg 49. *In* Luyendyk, B. P., Cann, J. R., et al, *Init. Repts. DSDP*, 49: Washington (U.S. Government Printing Office), 761-763. 10.2973/dsdp.proc.49.130.1979.

Clift, P. (2017) A revised budget for Cenozoic sedimentary carbon subduction. Rev. Geophys. 55, 97-125.

Coggon, R.M. and Teagle, D.A. (2011) Hydrothermal calcium-carbonate veins reveal past ocean chemistry. Trends Anal. Chem. 30, 1252-1268.

Coggon, R.M., Teagle, D.A., Cooper, M.J. and Vanko, D.A. (2004) Linking basement carbonate vein compositions to porewater geochemistry across the eastern flank of the Juan de Fuca Ridge, ODP Leg 168. Earth Planet. Sci. Lett. 219, 111-128.

Coggon, R.M., Teagle, D.A., Smith-Duque, C.E., Alt, J.C. and Cooper, M.J. (2010) Reconstructing past seawater Mg/Ca and Sr/Ca from mid-ocean ridge flank calcium carbonate veins. Science 327, 1114-1117.

Coggon, R.M., Teagle, D.A.H., Cooper, M.J., Hayes,, T.E.F. and Green, D.R.H. (2006) Data report: compositions of calcium carbonate veins from superfast spreading rate crust, ODP Leg 206. *In* Teagle, D.A.H., Wilson, D.S., Acton, G.D., and Vanko, D.A. (Eds.), 206: College Station, TX (Ocean Drilling Program), 1–6. 10.2973/odp.proc.sr.206.002.2006.

Coogan, L.A. and Gillis, K.M. (2013) Evidence that low ‐ temperature oceanic hydrothermal systems play an important role in the silicate ‐ carbonate weathering cycle and long ‐ term climate regulation. Geochem. Geophys. Geosyst. 14, 1771-1786.

Coogan, L.A., Parrish, R.R. and Roberts, N.M. (2016) Early hydrothermal carbon uptake by the upper oceanic crust: Insight from in situ U-Pb dating. Geology 44, 147-150.

Dasgupta, R. and Hirschmann, M.M. (2010) The deep carbon cycle and melting in Earth's interior. Earth Planet. Sci. Lett. 298, 1-13.

Dick, H.J., Schouten, H., Meyer, P.S., Gallo, D.G., Bergh, H., Tyce, R., Patriat, P., Johnson, K.T., Snow, J. and Fisher, A. (1991) Tectonic evolution of the Atlantis II fracture zone., In Von Herzen, R., Robinson, P.T., et al., Proc. ODP. Sci. Results, 118: College Station, TX (Ocean Drilling Program), 359-398., pp. 359-398.

Dilek, Y., Coulton, A. and Hurst, S.D. (1997) High-temperature ductile deformation of Site 920 peridotites. , in: Karson, J.A., Cannat, M., Miller, D.J., and Elthon, D. (Ed.), Proc. ODP, Sci. Results, 153: College Station, TX (Ocean Drilling Program), 23–34.

Dilek, Y. and Furnes, H. (2014) Ophiolites and their origins. Elements 10, 93-100.

Drummond Matthews. (1979) Shipboard measurements of seismic velocity, density, and porosity in DSDP Leg 46 basalts. *In* Dmitriev, L., Heirtzler, et al, *Init. Repts. DSDP*, 46: Washington (U.S. Government Printing Office), 379-382. 10.2973/dsdp.proc.46.128.1979.

Duncan, M.S. and Dasgupta, R. (2017) Rise of Earth’s atmospheric oxygen controlled by ecient subduction of organic carbon. Nature Geosci. 10, 387-391.

Expedition 309/312 Scientists. (2006) Site 1256. *In* Teagle, D.A.H., Alt, J.C., Umino, S., Miyashita, S., Banerjee, N.R., Wilson, D.S., and the Expedition 309/312 Scientists, *Proc. IODP*,

309/312: Washington, DC (Integrated Ocean Drilling Program Management International, Inc.), 1–549. 10.2204/iodp.proc.309312.103.2006.

Facq, S., Daniel, I., Montagnac, G., Cardon, H. and Sverjensky, D.A. (2014) In situ Raman study and thermodynamic model of aqueous carbonate speciation in equilibrium with aragonite under subduction zone conditions. Geochim. Cosmochim. Acta 132, 375-390.

Francheteau, J., Armijo, R., Cheminée, J., Hekinian, R., Lonsdale, P. and Blum, N. (1990) 1 Ma East Pacific Rise oceanic crust and uppermost mantle exposed by rifting in Hess Deep (equatorial Pacific Ocean). Earth Planet Sci. Lett. 101, 281-295.

Francois, L.M. and Walker, J.C. (1992) Modelling the Phanerozoic carbon cycle and climate: constraints from the 87Sr/86Sr isotopic ratio of seawater. Am. J. Sci 292, 81-135.

Froelich, P.N., Klinkhammer, G., Bender, M.L., Luedtke, N., Heath, G.R., Cullen, D., Dauphin, P., Hammond, D., Hartman, B. and Maynard, V. (1979) Early oxidation of organic matter in pelagic sediments of the eastern equatorial Atlantic: suboxic diagenesis. Geochim. Cosmochim. Acta. 43, 1075-1090.

Früh-Green, G.L., Kelley, D.S., Bernasconi, S.M., Karson, J.A., Ludwig, K.A., Butterfield, D.A., Boschi, C. and Proskurowski, G. (2003) 30,000 years of hydrothermal activity at the Lost City vent field. Science 301, 495-498.

Furnes, H., McLoughlin, N., Muehlenbachs, K., Banerjee, N., Staudigel, H., Dilek, Y., de Wit, M., Van Kranendonk, M. and Schiffman, P. (2008) Oceanic pillow lavas and hyaloclastites as habitats for microbial life through time–a review. *In* Links Between Geological Processes, Microbial Activities&Evolution of Life: Springer, 1-68.

Furnes, H., Muehlenbachs, K., Torsvik, T., Thorseth, I.H. and Tumyr, O. (2001) Microbial fractionation of carbon isotopes in altered basaltic glass from the Atlantic Ocean, Lau Basin and Costa Rica Rift. Chem. Geol. 173, 313-330.

Furnes, H., Muehlenbachs, K., Tumyr, O., Torsvik, T. and Thorseth, I.H. (1999) Depth of active bio-alteration in the ocean crust: Costa Rica Rift (Hole 504B). Terra Nova-Oxford 11, 228.

Furnes, H. and Staudigel, H. (1999) Biological mediation in ocean crust alteration: how deep is the deep biosphere? Earth Planet. Sci. Lett. 166, 97-103.

Galvez, M., Beyssac, O., Martinez, I. and Malavieille, J. (2013) Graphite formation by carbonate reduction during subduction. Nature Geosci. 6, 473-477.

Gillis, K. and Coogan, L. (2011) Secular variation in carbon uptake into the ocean crust. Earth Planet. Sci. Lett. 302, 385-392.

Goodenough, K.M., Thomas, R.J., Styles, M.T., Schofield, D.I. and MacLeod, C.J. (2014) Records of ocean growth and destruction in the Oman–UAE ophiolite. Elements 10, 109-114.

Gorman, P.J., Kerrick, D. and Connolly, J. (2006) Modeling open system metamorphic decarbonation of subducting slabs. Geochem. Geophys. Geosyst. 7.

Gregory, R.T. and Taylor, H.P. (1981) An oxygen isotope profile in a section of Cretaceous oceanic crust, Samail Ophiolite, Oman: Evidence for δ18O buffering of the oceans by deep (> 5 km) seawater - hydrothermal circulation at mid - ocean ridges. j. Geophys. Res. Solid Earth 86, 2737-2755.

Gudbrandsson, S., Wolff-Boenisch, D., Gislason, S.R. and Oelkers, E.H. (2011) An experimental study of crystalline basalt dissolution from 2⩽ pH⩽ 11 and temperatures from 5 to 75° C. Geochim. Cosmochim. Acta 75, 5496-5509.

Hart, S. and Staudigel, H. (1980) Ocean crust-sea water interaction: Sites 417 and 418. *In* Donnelly, T., Francheteau, J., Bryan, W., Robinson, P., Flower, M., Salisbury, M., et al, *Init. Rept. DSDP*, 51, 52, 53: (U.S. Government Printing Office), 1169-1176. 10.2973/dsdp.proc.515253.143.1980.

Hart, S.R., Blusztajn, J., Dick, H.J. and Lawrence, J.R. (1994) Fluid circulation in the oceanic crust: Contrast between volcanic and plutonic regimes. J. Geophys. Res. Solid Earth 99, 3163-3173.

Hasterok, D. (2013) A heat flow based cooling model for tectonic plates. Earth Planet. Sci. Lett. 361, 34-43.

Heimann, A., Johnson, C.M., Beard, B.L., Valley, J.W., Roden, E.E., Spicuzza, M.J. and Beukes, N.J. (2010) Fe, C, and O isotope compositions of banded iron formation carbonates demonstrate a major role for dissimilatory iron reduction in~ 2.5 Ga marine environments. Earth Planet Sci. Lett. 294, 8-18.

Huang, F., Daniel, I., Cardon, H., Montagnac, G. and Sverjensky, D.A. (2017) Immiscible hydrocarbon fluids in the deep carbon cycle. Nat. Commun. 8, 15798.

Humphris, S.E. and Thompson, G. (1978) Hydrothermal alteration of oceanic basalts by seawater. Geochim. Cosmochim. Acta 42, 107-125.

Ildefonse, B., Blackman, D., John, B., Ohara, Y., Miller, D. and MacLeod, C.J. (2007) Oceanic core complexes and crustal accretion at slow-spreading ridges. Geology 35, 623-626.

Jarrard, R.D. (2003) Subduction fluxes of water, carbon dioxide, chlorine, and potassium. Geochem. Geophys. Geosyst. 4, 8905.

Javoy, M. and Fouillac, A.M. (1978) Stable isotope ratios in Deep Sea Drilling Project Leg 51 basalts. In: T. Donnelly et al. (Editors),. Proc. ODP, Sci. Results., pp. 1153-1157.

Jiang, S., Wise, S. and Wang, Y. (2007) Cause of the middle/late Miocene carbonate crash: dissolution or low productivity? *In* Teagle, D.A.H., Wilson, D.S., Acton, G.D., and Vanko, D.A, *Proc. ODP, Sci, Results*, 206: College Station, TX (Ocean Drilling Program), 1-24.

Johnson, H.P. and Pruis, M.J. (2003) Fluxes of fluid and heat from the oceanic crustal reservoir. Earth Planet. Sci. Lett. 216, 565-574.

Jörg Erzinger. (1986) Basement geochemistry, Leg 92. *In* Leinen, M., Rea, D. K., et al, *Init. Repts. DSDP*, 92: Washington (U.S. Govt. Printing Office), 471-480. 10.2973/dsdp.proc.92.128.1986.

Jorgensen, B.B., Isaksen, M.F. and Jannasch, H.W. (1992) Bacterial sulfate reduction above 100 degrees Celsius in deep-sea hydrothermal vent sediments. Science 258, 1756-1758.

Karson, J.A. and Lawrence, R.M. (1997) Tetonic setting of serpentinite exposures on the western median valley wall of the MARK area in the vicinity of Site 920. *In* Karson, J.A., Cannat, M., Miller, D.J., and Elthon, D. (Eds.), *Proc. ODP, Sci. Results*, 153: College Station, TX (Ocean Drilling Program), 47-559.

Kashefi, K. and Lovley, D.R. (2003) Extending the upper temperature limit for life. Science 301, 934-934.

Kelemen, P.B., Koga, K. and Shimizu, N. (1997) Geochemistry of gabbro sills in the crust-mantle transition zone of the Oman ophiolite: Implications for the origin of the oceanic lower crust. Earth Planet Sci. Lett. 146, 475-488.

Kelemen, P.B. and Manning, C.E. (2015) Reevaluating carbon fluxes in subduction zones, what goes down, mostly comes up. Proc. Natl. Acad. Sci. 112, E3997-E4006.

Kenward, P.A., Goldstein, R.H., González, L.A. and Roberts, J.A. (2009) Precipitation of low-temperature dolomite from an anaerobic microbial consortium: the role of methanogenic Archaea. Geobiology 7, 556-565.

Kerrick, D. and Connolly, J. (2001a) Metamorphic devolatilization of subducted marine sediments and the transport of volatiles into the Earth's mantle. Nature 411, 293.

Kerrick, D. and Connolly, J. (2001b) Metamorphic devolatilization of subducted oceanic metabasalts: implications for seismicity, arc magmatism and volatile recycling. Earth planet. Sci. Lett. 189, 19-29.

Kim, S.-T. and O'Neil, J.R. (1997) Equilibrium and nonequilibrium oxygen isotope effects in synthetic carbonates. Geochim. Cosmochim. Acta 61, 3461-3475.

Kim, S.-T., O'Neil, J.R., Hillaire-Marcel, C. and Mucci, A. (2007) Oxygen isotope fractionation between synthetic aragonite and water: Influence of temperature and Mg^{2+} concentration. Geochim. Cosmochim. Acta 71, 4704-4715.

Laiginhas, F. (2008) Diamonds from the Ural Mountains: their characteristics and the mineralogy and geochemistry of their inclusions. University of Glasgow.

Lang, S.Q., Butterfield, D.A., Lilley, M.D., Johnson, H.P. and Hedges, J.I. (2006) Dissolved organic carbon in ridge-axis and ridge-flank hydrothermal systems. Geochim. Cosmochim. Acta 70, 3830-3842.

Lawrence, J. (1991) Stable isotopic composition of pore waters and calcite veins. *In* Weissel, J., Peirce, J., Taylor, E., and Alt, J., et al, *Proc. ODP, Sci. Results*, 121: College Station, TX (Ocean Drilling Program), 1-6.

Lawrence, J.R. (1980) Temperatures of formation of calcite veins in the basalts from Deep Sea Drilling Project Holes 417A and 417D. *In* Donnelly, T., Francheteau, J., Bryan, W., Robinson, P.,

Flower, M., Salisbury, M., et al, *Init. Repts. DSDP*, 51, 52, 53: (US Gov. Printing Office, Washington, DC), 1183-1184. 10.2973/dsdp.proc.515253.145.1980.

Leost, I., Stachel, T., Brey, G., Harris, J. and Ryabchikov, I. (2003) Diamond formation and source carbonation: mineral associations in diamonds from Namibia. Contrib. Mineral. Petrol. 145, 15-24.

Li, Z., Li, J., Lange, R., Liu, J. and Militzer, B. (2017) Determination of calcium carbonate and sodium carbonate melting curves up to Earth's transition zone pressures with implications for the deep carbon cycle. Earth Planet. Sci. Lett 457, 395-402.

Loh, A.N., Bauer, J.E. and Druffel, E.R. (2004) Variable ageing and storage of dissolved organic components in the open ocean. Nature 430, 877-881.

Mango, F.D. and Elrod, L. (1999) The carbon isotopic composition of catalytic gas: A comparative analysis with natural gas. Geochim. Cosmochim. Acta. 63, 1097-1106.

Mango, F.D. and Hightower, J. (1997) The catalytic decomposition of petroleum into natural gas. Geochim. Cosmochim. Acta. 61, 5347-5350.

McCarthy, M.D., Beaupré, S.R., Walker, B.D., Voparil, I., Guilderson, T.P. and Druffel, E.R. (2011) Chemosynthetic origin of 14C-depleted dissolved organic matter in a ridge-flank hydrothermal system. Nature Geosci. 4, 32-36.

McConnaughey, T. (1989a) 13C and 18O isotopic disequilibrium in biological carbonates: I. Patterns. Geochim. Cosmochim. Acta. 53, 151-162.

McConnaughey, T. (1989b) 13C and 18O isotopic disequilibrium in biological carbonates: II. In vitro simulation of kinetic isotope effects. Geochim. Cosmochim. Acta. 53, 163-171.

McConnaughey, T. (2003) Sub-equilibrium oxygen-18 and carbon-13 levels in biological carbonates: carbonate and kinetic models. Coral Reefs 22, 316-327.

McDermott, J.M., Seewald, J.S., German, C.R. and Sylva, S.P. (2015) Pathways for abiotic organic synthesis at submarine hydrothermal fields. Proc. Natl. Acad. Sci. 112, 7668-7672.

Merlini, M., Crichton, W.A., Hanfland, M., Gemmi, M., Müller, H., Kupenko, I. and Dubrovinsky, L. (2012) Structures of dolomite at ultrahigh pressure and their influence on the deep carbon cycle. Proc. Natl. Acad. Sci 109, 13509-13514.

Mikhail, S., Verchovsky, A.B., Howell, D., Hutchison, M., Southworth, R., Thomson, A., Warburton, P., Jones, A. and Milledge, H. (2014) Constraining the internal variability of the stable isotopes of carbon and nitrogen within mantle diamonds. Chem. Geol. 366, 14-23.

Molina, J.F. and Poli, S. (2000) Carbonate stability and fluid composition in subducted oceanic crust: an experimental study on H 2 O–CO 2-bearing basalts. Earth Planet. Sci. Lett. 176, 295-310.

Mortimer, R.J. and Coleman, M.L. (1997) Microbial influence on the oxygen isotopic composition of diagenetic siderite. Geochim. Cosmochim. Acta. 61, 1705-1711.

Mottl, M.J. and Wheat, C.G. (1994) Hydrothermal circulation through mid-ocean ridge flanks: Fluxes of heat and magnesium. Geochim. Cosmochim. Acta 58, 2225-2237.

Muehlenbachs, K. (1980) The alteration and aging of the basaltic layer of the sea floor: oxygen isotope evidence from DSDP/IODP Legs 51, 52, and 53. *In* Donnelly, T., Francheteau, J., Bryan, W., Robinson, P., Flower, M., Salisbury, M., et al, *Init. Rept. DSDP*, 53: Washington (U.S. Government Printing Office), 1159-1167. 10.2973/dsdp.proc.515253.142.1980.

Müller, R.D., Sdrolias, M., Gaina, C. and Roest, W.R. (2008) Age, spreading rates, and spreading asymmetry of the world's ocean crust. Geochem. Geophys. Geosyst. 9.

Natland, J., Tarney, J., Marsh, N., Melson, W. and OHearn, T. (1984) Compositions, stratigraphy, and alteration of pillow basalts, deep-sea drilling project Hole-543A, near the Barbados Ridge. *In* Biju-Duval, B., Moore, J. C, et al, *Init. Repts. DSDP*, 78: Washington (U.S. Govt. Printing Office), 393-399. 10.2973/dsdp.proc.78a.118.1984.

Natland, J.H. and Dick, H.J. (2002) Stratigraphy and composition of gabbros drilled in Ocean Drilling Program Hole 735B, Southwest Indian Ridge: a synthesis of geochemical data. In *In* Natland, J.H., Dich, H.J.B., Miller, D.J., and Von Herzen, R.P. (Eds.), *Proc. ODP, Sci. Results*, 176: college Station, TX (Ocean Drilling Program), 1-69. 10.2973/odp.proc.sr.176.002.2002.

O'Neil, J.R., Clayton, R.N. and Mayeda, T.K. (1969) Oxygen isotope fractionation in divalent metal carbonates. J. Chem. Phys. 51, 5547-5558.

Oberhansli, H. and Hemleben, C. (1984) Stable isotope record of the Pliocene and Pleistocene plantonic foraminifers from Leg 78A, Site 543, on the Baebados ridge complex. *In* Biju-Duval, B., Moore, J. C, *Init. Repts. DSDP*, 78A: Washington (U.S. Govt. Printing Office). 10.2973/dsdp.proc.78a.125.1984.

Palot, M., Cartigny, P., Harris, J., Kaminsky, F. and Stachel, T. (2012) Evidence for deep mantle convection and primordial heterogeneity from nitrogen and carbon stable isotopes in diamond. Earth Planet. Sci. Lett. 357, 179-193.

Palot, M., Cartigny, P. and Viljoen, F. (2009) Diamond origin and genesis: AC and N stable isotope study on diamonds from a single eclogitic xenolith (Kaalvallei, South Africa). Lithos 112, 758-766.

Palot, M., Pearson, D., Stern, R., Stachel, T. and Harris, J. (2014) Isotopic constraints on the nature and circulation of deep mantle C–H–O–N fluids: Carbon and nitrogen systematics within ultra-deep diamonds from Kankan (Guinea). Geochim. Cosmochim. Acta 139, 26-46.

Pan, D., Spanu, L., Harrison, B., Sverjensky, D.A. and Galli, G. (2013) Dielectric properties of water under extreme conditions and transport of carbonates in the deep Earth. Proc. Natl. Acad. Sci 110, 6646-6650.

Paul, H.J., Gillis, K.M., Coggon, R.M. and Teagle, D.A. (2006) ODP Site 1224: A missing link in the investigation of seafloor weathering. Geochem. Geophys. Geosyst 7.

Piccoli, F., Brovarone, A.V., Beyssac, O., Martinez, I., Ague, J.J. and Chaduteau, C. (2016) Carbonation by fluid–rock interactions at high-pressure conditions: Implications for carbon cycling in subduction zones. Earth Planet. Sci. Lett. 445, 146-159.

Plank, T. and Langmuir, C.H. (1998) The chemical composition of subducting sediment and its consequences for the crust and mantle. Chem. Geol. 145, 325-394.

Plümper, O., King, H.E., Geisler, T., Liu, Y., Pabst, S., Savov, I.P., Rost, D. and Zack, T. (2017) Subduction zone forearc serpentinites as incubators for deep microbial life. Proc. Natl. Acad. Sci. 114, 4324-4329.

Poli, S., Franzolin, E., Fumagalli, P. and Crottini, A. (2009) The transport of carbon and hydrogen in subducted oceanic crust: an experimental study to 5 GPa. Earth Planet. Sci. Lett. 278, 350-360.

Rohrbach, A., Ballhaus, C., Golla-Schindler, U., Ulmer, P., Kamenetsky, V.S. and Kuzmin, D.V. (2007) Metal saturation in the upper mantle. Nature 449, 456.

Rohrbach, A. and Schmidt, M.W. (2011) Redox freezing and melting in the Earth's deep mantle resulting from carbon-iron redox coupling. Nature 472, 209.

Rollion-Bard, C., Chaussidon, M. and France-Lanord, C. (2003) pH control on oxygen isotopic composition of symbiotic corals. Earth Planet. Sci. Lett. 215, 275-288.

Ryan, W.B., Carbotte, S.M., Coplan, J.O., O'Hara, S., Melkonian, A., Arko, R., Weissel, R.A., Ferrini, V., Goodwillie, A. and Nitsche, F. (2009) Global multi‐resolution topography synthesis. Geochem. Geophys. Geosyst. 10.

Schwarzenbach, E.M., Früh-Green, G.L., Bernasconi, S.M., Alt, J.C. and Plas, A. (2013) Serpentinization and carbon sequestration: A study of two ancient peridotite-hosted hydrothermal systems. Chem. Geol. 351, 115-133.

Searle, M. and Cox, J. (1999) Tectonic setting, origin, and obduction of the Oman ophiolite. Geol. Soc. Am. Bull. 111, 104-122.

Seyfried Jr, W. (1987) Experimental and theoretical constraints on hydrothermal alteration processes at mid-ocean ridges. Annu. Rev. Earth Planet. Sci. 15, 317-335.

Shilobreeva, S., Martinez, I., Busigny, V., Agrinier, P. and Laverne, C. (2011) Insights into C and H storage in the altered oceanic crust: Results from ODP/IODP Hole 1256D. Geochim. Cosmochim. Acta. 75, 2237-2255.

Shipboard scientific Party. (1977) Site 332. *In* Aumento, F., Melson, W. G. et al, *Init. Repts. DSDP*, 37: Part 1: Washington(U.S. Government Printing Office), 15-199. 10.2973/dsdp.proc.37.102.1977.

Shipboard Scientific Party. (1979a) Site 410. *In* Luyendyk, B. P., Cann, J. R., et al, *Init. Repts. DSDP*, 49: Washington (U.S. Government Printing Office), 227-313. 10.2973/dsdp.proc.49.105.1979.

Shipboard Scientific Party. (1979b) Site 411. *In* Luyendyk, B. P., Cann, J. R., et al, *Init. Repts. DSDP*, 49: Washington (U.S. Government Printing Office), 315-338. 10.2973/dsdp.proc.49.106.1979.

Shipboard Scientific Party. (1984) Site 543: Oceanic reference site east of the Barbados Ridge Complex. iNITIAL Reports of the Deep Sea Drilling Project, 227-298.

Shipboard Scientific Party. (1985a) Site 556. *In* Bougault, H., Cande, S. C, et al, *Init. Repts. DSDP*, 82: Washington (U.S. Govt. Printing Office), 61-113. 10.2973/dsdp.proc.82.105.1985.

Shipboard Scientific Party. (1985b) Site 562. *In* Bougault, H., Cande, S. C, et al, *Init. Repts. DSDP*, 82: Washington (U.S. Govt. Printing Office), 591-603. 10.2973/dsdp.proc.82.111.1985.

Shipboard Scientific Party. (1986) Site 597. *In* Leinen, M., Rea, D. K., et al, *Init. Repts. DSDP*, 92: Washington (U.S. Govt. Printing Office), 25-96. 10.2973/dsdp.proc.92.102.1986.

Shipboard Scientific Party. (1990) Site 801. *In* Lancelot, Y., Larson, R.L., et al, *Proc. ODP, Init. Repts*, 129: College Station, TX (Ocean Drilling Program), 91–170. 10.2973/odp.proc.ir.129.103.1990.

Shipboard Scientific Party. (1992) Site 843. *In* Dziewonski, A., Wilkens, R., Firth, J., et al, *Proc. ODP, Init. Repts*, 136: College Station, TX (Ocean Drilling Program), 65–99. 10.2973/odp.proc.ir.136.105.1992.

Shipboard Scientific Party. (1993a) Site 504. *In* Alt, J.C., Kinoshita, H., Stokking, L.B., et al, *Proc. ODP, Init. Repts*, 148: College Station, TX (Ocean Drilling Program), 27-121. 10.2973/odp.proc.ir.148.102.1993.

Shipboard Scientific Party. (1993b) Site 896. *In* Alt, J.C., Kinoshita, H., Stokking, L.B., et al, *Proc. ODP, Init. Repts*, 148: College Station, TX (Ocean Drilling Program), 123–192. 10.2973/odp.proc.ir.148.103.1993.

Shipboard Scientific Party. (1995), In Cannat, M., Karson, J.A., Miller, D.J., et al., Proc. ODP, Init. Repts, 153: College Station, TX (Ocean Drilling Program), 45-119.

Shipboard Scientific Party. (2000) Site 801. *In* Plank, T., Ludden, J.N., Escutia, C., et al, *Proc. ODP, Init. Repts*, 185: College Station, TX (Ocean Drilling Program), 1–222. 10.2973/odp.proc.ir.185.103.2000.

Shipboard Scientific Party. (2003a) Leg 206 summary. *In* Wilson, D.S., Teagle, D.A.H., Acton, G.D., et al, *Proc. ODP, Init*, 206: College Station, TX (Ocean Drilling Program), 1–117. 10.2973/odp.proc.ir.206.101.2003.

Shipboard Scientific Party. (2003b) Site 1224. *In* Stephen, R.A., Kasahara, J., Acton, G.D., et al, *Proc. ODP, Sci. Results*, 200: College Station, TX (Ocean Drilling Program), 1–178. 10.2973/odp.proc.ir.200.104.2003.

Shipboard Scientific Party. (2004) Site 1268. *In* Kelemen, P.B., Kikawa, E., Miller, D.J., et al, *Proc. ODP, Init. Repts*, 209: College Station, TX (Ocean Drilling Program), 1–171.

Stachel, T., Harris, J., Aulbach, S. and Deines, P. (2002) Kankan diamonds (Guinea) III: d 13 C and nitrogen characteristics of deep diamonds. Contrib. Miner. Petrol. 142, 465-475.

Stachel, T., Harris, J.W. and Muehlenbachs, K. (2009) Sources of carbon in inclusion bearing diamonds. Lithos 112, 625-637.

Staudigel, H. (2003) Hydrothermal alteration processes in the oceanic crust. Treatise on geochemistry 3, 659.

Staudigel, H., Davies, G., Hart, S.R., Marchant, K. and Smith, B.M. (1995) Large scale isotopic Sr, Nd and O isotopic anatomy of altered oceanic crust: DSDP/ODP sites417/418. Earth Planet. Sci. Lett. 130, 169-185.

Staudigel, H., Hart, S.R. and Richardson, S.H. (1981) Alteration of the oceanic crust: processes and timing. Earth Planet Sci. Lett. 52, 311-327.

Staudigel, H., Hart, S.R., Schmincke, H.-U. and Smith, B.M. (1989) Cretaceous ocean crust at DSDP Sites 417 and 418: Carbon uptake from weathering versus loss by magmatic outgassing. Geochim. Cosmochim. Acta. 53, 3091-3094.

Staudigel, H., Kastner, M. and Sturz, A. (1986) $\delta^{18}O$ and $^{87}Sr/^{86}Sr$ of Calcites from the Basaltic Basement of Deep Sea Drilling Project Site 597: Timing and Temperature of Alteration. *In* Leinen, M., Rea, D. K., et al, *Init. Repts. DSDP*, 92: Washington (U.S. Govt. Printing Office), 499-503. 10.2973/dsdp.proc.92.131.1986.

Stein, C.A. and Stein, S. (1992) A model for the global variation in oceanic depth and heat flow with lithospheric age. Nature 359.

Stein, C.A. and Stein, S. (1994) Constraints on hydrothermal heat flux through the oceanic lithosphere from global heat flow. J. Geophys. Res. Solid Earth 99, 3081-3095.

Sumner, D.Y. (2001) Microbial influences on local carbon isotopic ratios and their preservation in carbonate. Astrobiology 1, 57-70.

Sverjensky, D.A., Stagno, V. and Huang, F. (2014) Important role for organic carbon in subduction-zone fluids in the deep carbon cycle. Nature Geosci. 7, 909.

Tappert, R., Stachel, T., Harris, J.W., Muehlenbachs, K., Ludwig, T. and Brey, G.P. (2005) Subducting oceanic crust: The source of deep diamonds. Geology 33, 565-568.

Teagle, D.A.H., Alt, J.C., Bach, W., Halliday, A.N. and Erzinger, J. (1996) Alteration of upper ocean crust in a ridge-flank hydrothermal upflow zone: mineral, chemical, and isotopic constraints from Hole 896A. *In* Alt, J.C., Kinoshita, H., Stokking, L.B., and Michael, P.J (Eds.), *Proc. ODP, Sci. Results*, 148: College Station, TX (Ocean Drilling Program). 10.2973/odp.proc.sr.148.113.

Thaler, C., Millo, C., Ader, M., Chaduteau, C., Guyot, F. and Ménez, B. (2017) Disequilibrium δ 18 O values in microbial carbonates as a tracer of metabolic production of dissolved inorganic carbon. Geochim. Cosmochim. Acta. 199, 112-129.

Thomassot, E., Cartigny, P., Harris, J., Lorand, J., Rollion-Bard, C. and Chaussidon, M. (2009) Metasomatic diamond growth: A multi-isotope study (13 C, 15 N, 33 S, 34 S) of sulphide inclusions and their host diamonds from Jwaneng (Botswana). Earth Planet. Sci. Lett. 282, 79-90.

Thomson, A.R., Walter, M.J., Kohn, S.C. and Brooker, R.A. (2016) Slab melting as a barrier to deep carbon subduction. Nature 529, 76-79.

Thornton, E.R. (1962) Solvent isotope effects in H2O16 and H2O18. Journal of the American Chemical Society 84, 2474-2475.

Tilton, G., Hopson, C. and Wright, J. (1981) Uranium ‐ lead isotopic ages of the Samail Ophiolite, Oman, with applications to Tethyan ocean ridge tectonics. J. Geophys. Res. Solid Earth 86, 2763-2775.

Torsvik, T., Furnes, H., Muehlenbachs, K., Thorseth, I.H. and Tumyr, O. (1998) Evidence for microbial activity at the glass-alteration interface in oceanic basalts. Earth Planet. Sci. Lett. 162, 165-176.

Tucholke, B.E. and Lin, J. (1994) A geological model for the structure of ridge segments in slow spreading ocean crust. J. Geophys. Res. Solid Earth 99, 11937-11958.

Tucholke, B.E., Lin, J. and Kleinrock, M.C. (1998) Megamullions and mullion structure defining oceanic metamorphic core complexes on the Mid‐Atlantic Ridge. J. Geophys. Res. Solid Earth 103, 9857-9866.

Van Heerden, L.A., Boyd, S.B., Milledge, J.H. and Pillinger, C.T. (1995) The carbon and nitrogen-isotope characteristics of the Argyle and Ellendale diamonds, Western Australia. Int. Geol. Rev. 37, 39-50.

Van Lith, Y., Warthmann, R., Vasconcelos, C. and Mckenzie, J.A. (2003) Sulphate‐reducing bacteria induce low‐temperature Ca‐dolomite and high Mg‐calcite formation. Geobiology 1, 71-79.

Visscher, P.T., Reid, R.P. and Bebout, B.M. (2000) Microscale observations of sulfate reduction: correlation of microbial activity with lithified micritic laminae in modern marine stromatolites. Geology 28, 919-922.

Visscher, P.T., Reid, R.P., Bebout, B.M., Hoeft, S.E., Macintyre, I.G. and Thompson, J.A. (1998) Formation of lithified micritic laminae in modern marine stromatolites (Bahamas): the role of sulfur cycling. Am. Mineral 83, 1482-1493.

von Breymann, M.t. and Berner, U. (1991) Isotopic Characterization of Secondary Carbonates from Sulu and Celebes Sea Basalts: Contrasting Scenarios of Basalt-Seawater Interaction. *In* Silver, E.A., Rangin, C., von Breymann, M.T., et al, *Proc. ODP, Sci. Results*, 124: College Station, TX (Ocean Drilling Program), 203–215. doi:10.2973/odp.proc.sr.124.154.1991.

Walter, M., Kohn, S., Araujo, D., Bulanova, G., Smith, C., Gaillou, E., Wang, J., Steele, A. and Shirey, S. (2011) Deep mantle cycling of oceanic crust: evidence from diamonds and their mineral inclusions. Science 334, 54-57.

Watkins, J.M., Nielsen, L.C., Ryerson, F.J. and DePaolo, D.J. (2013) The influence of kinetics on the oxygen isotope composition of calcium carbonate. Earth Planet. Sci. Lett. 375, 349-360.

Wilson, D.S., Teagle, D.A., Alt, J.C., Banerjee, N.R., Umino, S., Miyashita, S., Acton, G.D., Anma, R., Barr, S.R. and Belghoul, A. (2006) Drilling to gabbro in intact ocean crust. science 312, 1016-1020.

Wolff-Boenisch, D., Gislason, S.R. and Oelkers, E.H. (2006) The effect of crystallinity on dissolution rates and CO 2 consumption capacity of silicates. Geochim. Cosmochim. Acta 70, 858-870.

Zhang, C., Wang, L.-X., Marks, M.A., France, L. and Koepke, J. (2017) Volatiles (CO 2, S, F, Cl, Br) in the dike-gabbro transition zone at IODP Hole 1256D: Magmatic imprint versus hydrothermal influence at fast-spreading mid-ocean ridge. Chem. Geol. 459, 43-60.

Zheng, Y.-F. and Hoefs, J. (1993) Carbon and oxygen isotopic covariations in hydrothermal calcites. Miner. Depos. 28, 79-89.